Article:
Dipon Ghosh, D, Sanders, T, Hong, S et al. (5 more authors) (2016) Neural Architecture of Hunger-Dependent Multisensory Decision Making in C. elegans. Neuron, 92 (5). pp. 1049-1062. ISSN 0896-6273

https://doi.org/10.1016/j.neuron.2016.10.030

Neural architecture of hunger-dependent multisensory decision making in C. elegans

D. Dipon Ghosh[1], Tom Sanders[2], Soonwook Hong[1], Li Yan McCurdy[1,3], Daniel L. Chase[4], Netta Cohen[2], Michael R. Koelle[5], and Michael N. Nitabach[1,6,7,8,9]

[1]Department of Cellular and Molecular Physiology, Yale University, New Haven, CT

[2]School of Computing, University of Leeds, Leeds LS2 9JT, United Kingdom

[3]Interdepartmental Neuroscience Program, Yale University, New Haven, CT

[4]Department of Biomolecular Sciences, Central Connecticut State University, New Britain, CT

[5]Department of Molecular Biophysics and Biochemistry, Yale University, New Haven, CT

[6]Department of Genetics, Yale University, New Haven, CT

[7]Program in Cellular Neuroscience, Neurodegeneration and Repair, Yale University, New Haven, CT

[8]Corresponding author: michael.nitabach@yale.edu

[9]Lead contact: michael.nitabach@yale.edu

SUMMARY

Little is known about how animals integrate multiple sensory inputs in natural environments to balance avoidance of danger with approach to things of value. Furthermore, the mechanistic link between internal physiological state and threat-reward decision making remains poorly understood. Here we confronted C. elegans worms with the decision whether to cross a hyperosmotic barrier presenting the threat of desiccation to reach a source of food odor. We identified a specific interneuron that controls this decision via top-down extrasynaptic aminergic potentiation of the primary osmosensory neurons to increase their sensitivity to the barrier. We also establish that food deprivation increases the worm's willingness to cross the dangerous barrier by suppressing this pathway. These studies reveal a potentially general neural circuit architecture for internal state control of threat-reward decision making.

INTRODUCTION

Animals navigate complex natural environments containing both dangerous and valuable items, such as predators and food. The sensory cues that signal danger and reward are frequently transduced by different senses. In such circumstances, multisensory decision processes survey internal physiological state and balance attention to relevant sensory modalities to drive behavioral outputs (Rangel et al., 2008; Talsma et al., 2010). In human beings and other mammals, a key motif of multisensory integration is "top-down" control of perception (Manita et al., 2015; Talsma et al., 2010), wherein primary sensory cortex activity is modulated by feedback from higher-order regions (Fairhall and Macaluso, 2009; Fu et al., 2014; Zhang et al., 2014). Top-down control directs attention to the sensory modality signaling the most important features of a noisy environment given current internal physiological state (Berthoud, 2011; Rangel et al., 2008; Talsma, 2015). However, cellular and molecular mechanisms underlying internal state-dependent top-down attentional control in the context of threat-reward decision making remain unknown.

Here we employ the nematode worm Caenorhabditis elegans as a model system to investigate the molecular and cellular basis of multisensory decision making. In its natural environment in decomposing organic matter (Frezal and Felix, 2015), C. elegans must approach and obtain food while avoiding various threats, which include toxic chemicals and hyperosmotic concentrations of otherwise innocuous solutes. Worms detect threat and reward via primary sensory neurons that then propagate such information through an interneuron network to ultimately reach premotor command interneurons that direct locomotion (**Figure 1A**) (Varshney et al., 2011; White et al., 1986). The attractive food odor diacetyl is detected by the bilateral chemosensory neuron pair AWA (Sengupta et al., 1996). Avervise hyperosmolarity—which can

induce damage and death by desiccation (Culotti and Russell, 1978; Solomon et al., 2004)—is detected by the bilateral polymodal sensory neuron pair ASH (Hilliard et al., 2005; Kaplan and Horvitz, 1993). AWA and ASH propagate their sensory responses to an interconnected network of sensory interneurons (Ishihara et al., 2002; Luo et al., 2014; Shinkai et al., 2011). These sensory interneurons then provide inputs to the bilateral pair of RIM sensorimotor interneurons (Gordus et al., 2015; Guo et al., 2009; Piggott et al., 2011; White et al., 1986). RIM receives inhibitory synaptic inputs from sensory interneurons activated by attractive odors, such as diacetyl transduced by AWA (Gordus et al., 2015; Li et al., 2012). RIM receives excitatory synaptic inputs from sensory interneurons activated by aversive stimuli, such as hyperosmolarity transduced by ASH (Guo et al., 2009; Piggott et al., 2011). RIM, in turn, provides inhibitory synaptic inputs to forward command interneurons (Kawano et al., 2011; Pirri et al., 2009) and excitatory synaptic and gap-junction-coupled inputs to backward command interneurons (Gordus et al., 2015; Guo et al., 2009). This sensorimotor network topology and the signs of its synaptic connections ensure that aversive stimuli bias the worm towards backing up and changing direction, while attractive stimuli bias the worm towards continued forward motion. ASH also directly excites backward command interneurons, thus providing an alternative parallel feedforward pathway by which it can induce avoidance of danger (Guo et al., 2009).

Previous studies have implicated the AIY sensory interneurons in setting the multisensory threat-reward decision balance of approach to the attractive odor diacetyl when confronting a toxic Cu^{2+} barrier (Ishihara et al., 2002; Shinkai et al., 2011). Specifically, HEN-1 protein secreted by AIY acts on its receptor SCD-2 in another sensory interneuron pair AIA to regulate the decision to cross the Cu^{2+} barrier (Ishihara et al., 2002; Shinkai et al., 2011). Dopamine also regulates this threat-reward decision (Wang et al., 2014). While food deprivation

increases threat tolerance in this multisensory decision, the HEN-1 and dopamine receptor pathways are dispensable for this hunger effect (Ishihara et al., 2002; Wang et al., 2014). Thus, cellular and molecular mechanisms by which internal physiological state modulates threat-reward decision making in C. elegans, or indeed, any animal, remain unknown.

As discussed above, RIM is suitably positioned within the sensorimotor control network to regulate multisensory threat-reward decision making. RIM expresses the neuropeptide Pigment Dispersing Factor-2 (PDF-2) and its cognate G protein-coupled receptor (GPCR), PDFR-1 (Flavell et al., 2013; Janssen et al., 2008; Janssen et al., 2009; Meelkop et al., 2012). While PDF-1, another ligand of PDFR-1, has recently been shown to play a role in arousal-related behaviors (Barrios et al., 2012; Choi et al., 2013; Flavell et al., 2013), PDF-2 function is not well characterized. We found that PDFR-1 activation by PDF-2 in RIM decreases threat tolerance in the multisensory decision task. Unexpectedly, RIM does not control the decision via its known synaptic connections within the sensorimotor control network. Rather, RIM controls the decision by previously unknown extrasynaptic top-down tyraminergic positive feedback onto the primary osmosensory ASH neurons. Our results also indicate that internal hunger state suppresses this positive feedback loop, thereby increasing threat tolerance of food-deprived worms. These studies reveal underlying molecular and cellular mechanisms of internal state control of multisensory threat-reward decision making in the worm, and suggest that top-down topological motifs of multisensory integration are similar in mammals and the vastly simpler worm.

RESULTS

Hunger modulates multisensory threat-reward decision making

To provide a controlled behavioral context for exploring mechanisms underlying multisensory decision making, we employed a task in which worms balance danger of osmotic dessication with reward of food. A 1 cm diameter hyperosmotic fructose barrier ring is applied to a 5 cm diameter agar plate without food, and two 1 µL spots of diluted diacetyl food odor are applied outside the ring (**Figure 1B**). After allowing five minutes for the hyperosmotic solution to absorb into the agar and diffuse to establish an osmotic gradient, ten worms are removed from food-containing plates and placed in the center of the ring (**Figure 1B**). The decision balance between retreating from versus exiting the barrier ring is quantified as the fraction of worms that exit the ring within 15 minutes of being placed.

Approximately 30% of worms exit a 2 M fructose ring in the absence of food odor (**Figure 1C**), driven by their intrinsic propensity to disperse (Culotti and Russell, 1978; Gray et al., 2005). The presence of two 1 µl drops of 1:350 dilution of diacetyl in water outside the ring increases exiting to 80% (**Figure 1C**). This increase in exiting is abolished in odr-10 null-mutant worms that lack the ODR-10 diacetyl receptor (Sengupta et al., 1996) (**Figure 1C**). Spots of more diluted diacetyl result in smaller increases in exiting (data not shown). Increasing the fructose ring concentration to 3 M abolishes exiting even in the presence of food odor (**Figure 1D**). To determine if internal physiological state modulates this multisensory threat-reward decision, we deprived worms of food before testing. The decisions of worms deprived of food for fifteen minutes are indistinguishable from those of non-deprived worms (**Figure 1D**). In

contrast, worms deprived of food for one hour increase exiting relative to non-deprived worms, and worms deprived of food for five hours increase exiting even further (**Figure 1D**).

PDF-2 neuropeptide regulates multisensory decision making

As discussed above, the position of RIM in the sensorimotor control network is suitable for controlling multisensory threat-reward decision making (**Figure 1A**). While multiple neurons express either PDF-2 or its receptor PDFR-1, RIM expresses both (**Figure 2A**). PDF-1 and PDFR-1 null-mutant worms exhibit locomotor defects (Janssen et al., 2008; Meelkop et al., 2012) attributable to altered arousal state (Barrios et al., 2012; Choi et al., 2013; Flavell et al., 2013) that preclude testing in the multisensory decision assay. However, pdf-2 null-mutant worms exhibit grossly normal locomotion (see below), allowing us to test whether the balance of threat-reward decision making is altered in pdf-2 null-mutant worms. While wild-type worms readily exit a 2 M fructose ring to approach the source of food odor, they are almost completely contained by a 3 M ring (**Figure 2B**). In contrast, pdf-2 null-mutant worms readily exit the 3 M ring to approach the source of food odor, although they are still contained by a 4 M ring (**Figure 2B**). Complete rescue of the wild-type decision balance by transgenic re-expression of pdf-2 under the control of its own promoter sequence establishes the absence of PDF-2 peptide as the cause of the pdf-2 null-mutant decision phenotype (**Figure 2B**). Interestingly, the pdf-2 null mutation has no effect on avoidance of the osmotic ring in the absence of diacetyl, nor on attraction to diacetyl in the absence of the osmotic ring (**Figure 2B, C, D**). This absence of unisensory defects rules out primary sensory defects and suggests a specific role for PDF-2 in multisensory decision making.

To determine whether the pdf-2 null mutation causes a general defect in locomotion in the multisensory decision paradigm, we used automated worm tracking to directly measure locomotor kinematics as worms navigate within the osmotic ring (**Figure 2E**). The radial distribution of pdf-2 null-mutant worm trajectories was quantified during the first five minutes of the assay (before any pdf-2 null-mutant worms exit the ring). Trajectories of pdf-2 null-mutant worms are indistinguishable from wild-type worms (**Figure 2F**). There is also no detectable effect of the pdf-2 null mutation on standard locomotor kinematic parameters, including reversal frequency, high angle "omega turn" frequency, reversal magnitude, and forward bout duration (**Figure S1B**). Exiting in the absence of food odor is unaffected in pdf-2 null-mutant worms (**Figure 2B, C**), and there is no statistically significant effect of the pdf-2 null mutation on locomotor kinematics within the ring in this unisensory context (**Figure S1C, D**). Taken together, these results indicate that a general defect in locomotion—such as might prevent reversal and retreat upon approaching the hyperosmotic ring—cannot account for the altered multisensory decision balance of pdf-2 null-mutant worms.

PDF-2 acts on PDFR-1 in RIM to set the threat-reward decision balance

We next sought to determine both the cellular origin and target site of action of PDF-2 in regulating the threat-reward decision. Targeted re-expression of pdf-2 in pdf-2 null-mutant worms using a promoter specific to RIM and RIC, another interneuron pair near RIM in the anterior nerve ring (White et al., 1986), fully rescues the multisensory decision (**Figure 3A**). While only RIM normally expresses PDF-2 (Janssen et al., 2009), this indicates that PDF-2 secretion by RIM and RIC is sufficient to mediate wild-type decision balance. To determine the relevant PDFR-1-expressing targets of PDF-2, we employed membrane-tethered PDF-2 peptide (t-PDF-2) to activate PDFR-1 in specific neurons (**Figure 3B**). This approach has been

extensively validated in vitro and in vivo for cell-autonomous pharmacologically specific sustained activation of Drosophila PDFR and other class B1 neuropeptide receptors (Choi et al., 2012; Choi et al., 2009; Fortin et al., 2009; Krupp et al., 2013; Kunst et al., 2014). As noted earlier, RIM also expresses the PDF-2-receptor PDFR-1. Expression of t-PDF-2 in pdf-2 null-mutant worms using either of two promoters whose expression overlaps solely in RIM fully rescues the decision balance (**Figure 3C**). Expression of t-PDF-2 in RIC, which does not express PDFR-1 (Barrios et al., 2012; Flavell et al., 2013; Janssen et al., 2008), and expression of a sequence-scrambled version of the tethered peptide (t-SCR) in RIM each fail to rescue the decision phenotype (**Figure 3C**). This confirms the cell-autonomy and pharmacological specificity of t-PDF-2 activation of PDFR-1 in RIM. Finally, expression of t-PDF-2 in RIM and RIC in a wild-type background does not suppress exiting of a 2 M fructose ring in the presence of diacetyl, suggesting that the PDF-2-PDFR-1 autocrine loop is maximally active in this state, thereby precluding any gain-of-function t-PDF-2 effect (**Figure S2**). Taken together, these data indicate that PDF-2 secretion by RIM and RIC and autocrine action of PDF-2 on PDFR-1 in RIM are each sufficient to mediate a wild-type decision balance, and establish RIM as a key locus of control of multisensory decision making in the worm.

Tyraminergic positive feedback from RIM to ASH sets the threat-reward decision balance

How does PDFR-1 activation in RIM decrease threat tolerance in the approach to food? One way in which RIM communicates with its downstream targets is via secretion of the biogenic amine tyramine, which is synthesized from tyrosine in a reaction catalyzed by the enzyme tyrosine decarboxylase (TDC), encoded by the tdc-1 gene (**Figure 3D**) (Alkema et al., 2005). tdc-1 null-mutant worms lack tyramine and phenocopy the pdf-2 null-mutant phenotype, with worms now readily exiting the 3 M ring to approach the source of food odor, and with

unaltered avoidance of the osmotic ring on its own (**Figure 3E**). As for pdf-2 null-mutant worms, locomotor kinematic defects do not account for the altered threat-reward decision balance of tdc-1 null-mutant worms (**Figure S1**). tdc-1 null-mutant worms also lack the biogenic amine octopamine, which is synthesized from tyramine in a reaction catalyzed by tyramine β-hydroxylase (TBH), encoded by the tbh-1 gene (**Figure 3D**) (Alkema et al., 2005). However, tbh-1 null-mutant worms, which synthesize tyramine but lack octopamine (Alkema et al., 2005), are unaffected (**Figure 3E**). This establishes that tyramine, and not octopamine, regulates the threat-reward decision balance. Additionally, double null-mutant pdf-2; tdc-1 worms behave identically to both pdf-2 and tdc-1 single-mutant worms, suggesting that these genes function in the same genetic pathway to control the decision (**Figure 3E**). Finally, targeted re-expression of tdc-1 in tdc-1 null-mutant worms in RIM and RIC, but not RIC alone, fully rescues the multisensory decision (**Figure 3F**). RIM is the only tyraminergic neuron in the sensorimotor control network (Alkema et al., 2005; Donnelly et al., 2013; Pirri et al., 2009), and the only other tyraminergic neuroendocrine cell in the worm, uv1, controls egg-laying (Alkema et al., 2005; Jose et al., 2007). Taken together with the key role of PDFR-1 activation in RIM (**Figure 3C**), these results strongly support the conclusion that RIM controls threat-reward decision making, and that it exerts this control via tyraminergic signaling to tyramine receptor-expressing targets.

What is the relevant tyramine receptor, and where and how does it act to mediate RIM control of the threat-reward decision balance? The worm genome encodes a hyperpolarizing tyramine-gated Cl^- channel (LGC-55) expressed in one of the forward command interneurons, and previously shown to regulate locomotion (Pirri et al., 2009), as well as several tyramine GPCRs related to vertebrate adrenergic receptors, including TYRA-2, SER-2, and TYRA-3 (Donnelly et al., 2013; Rex and Komuniecki, 2002; Rex et al., 2004; Wragg et al., 2007). We

considered LGC-55 a particularly likely target of RIM tyramine signals in the control of threat-reward decision making, as it mediates direct synaptic inhibition of forward locomotor command interneurons by RIM (Alkema et al., 2005; Pirri et al., 2009). However, the threat-reward decision balance of both lgc-55 and tyra-3 null-mutant worms is indistinguishable from that of the wild-type (**Figure 4A**). ser-2 null-mutant worms possibly exhibit altered multisensory decision balance, although not statistically distinguishable from the wild-type in our assays. ser-2 null-mutant worms also exit the 3 M fructose ring in the absence of food odor more readily than wild-type, which could potentially be explained by previously described defects in avoidance and turning behaviors (Donnelly et al., 2013; Rex et al., 2004) (**Figure 4A**). Unlike the other tyramine receptor null-mutant worms, however, tyra-2 null-mutant worms readily exit a 3 M ring to approach the source of food odor, phenocopying both pdf-2 and tdc-1 null-mutant worms (**Figure 4A**). Like pdf-2 and tdc-1 null-mutant worms, tyra-2 null-mutant worms are unaffected in the unisensory avoidance-only context (**Figure 4A**). Furthermore, double null-mutant pdf-2; tyra-2 worms behave identically to both pdf-2 and tyra-2 single-mutant worms, suggesting that these signaling modules operate in the same functional pathway to determine threat-reward decision balance (**Figure 4A**). Little is known about tyra-2 function (Donnelly et al., 2013; Jin et al., 2016; Pirri et al., 2009; Rex et al., 2005), and our results now demonstrate that TYRA-2 is the receptor through which tyramine secreted by RIM controls threat-reward decision making.

tyra-2 is expressed in a number of sensory neurons, including the osmosensory neuron ASH (Rex et al., 2005). Re-expression of tyra-2 using either of two cell-specific promoters whose expression overlaps only in ASH rescues the wild-type decision balance in tyra-2 null-mutant worms, while re-expression using a promoter active in other sensory neurons but not ASH has no effect (**Figure 4B**). Functional imaging of ASH Ca^{2+} responses to osmotic stimuli

revealed that exogenous tyramine pre-treatment increases ASH osmosensitivity, indicating neuronal activation (**Figure 4C, D, E**) (Zahratka et al., 2015). Tyramine potentiation of ASH osmosensitivity is abolished in *tyra-2* null-mutant worms (**Figure 4F, G, H**). Finally, we compared the time it takes *tyra-2* null-mutant worms to exit the ring in the standard multisensory assay and a time-shifted configuration in which the fructose ring is allowed five extra minutes to diffuse before the worms are placed (**Figure S3A**). Worm begin to exit the time-shifted configuration immediately after being placed, while worms begin to exit in the standard assay about five minutes after being placed (**Figure S3B, S3C**). Therefore exiting in the threat-reward decision assay is determined by the state of the osmotic barrier as each worm confronts it and the osmosensitivity of the ASH neuron as regulated by tyraminergic feedback (**Figure S3B, S3C, S3D**). As RIM does not form synapses onto ASH (although ASH does synapse onto RIM) (White et al., 1986), taken together these results demonstrate that RIM controls multisensory threat-reward decision making by secreting tyramine to act extrasynaptically at a distance directly on ASH through TYRA-2 to potentiate ASH sensitivity to osmotic stimuli.

Computational modeling predicts slow, non-linear tyramine regulation of threat-reward decision making

To characterize the interplay between neural activity, neuromodulatory activity, behavior, and the environment, we modeled each of these dynamic components *in silico* (Cohen and Sanders, 2014). Model worms contain a highly simplified minimal nervous system sufficient for decision making (**Figure 5A**; see **Experimental Procedures** and **Supplemental Methods** for details). Model parameters were fit to match the experimental exiting rates of **Figure 2B**. To illustrate the temporal evolution of the decision process, we plotted the locomotor trajectories and neural and neuromodulatory activity underlying the behavior of example simulated wild-type and *tyra-2* null-mutant worms

(**Figure 5C, D**). This reveals that oscillatory changes in fructose and diacetyl concentration experienced by the worm as it undulates within the arena (**Figure 5C**) induce corresponding oscillatory changes in the activity of AWA, ASH, and RIM (**Figure 5D**) that are phase locked to the undulatory locomotor DMN-VMN pattern generator. In both wild-type and tyra-2 null-mutant worms, the magnitude of RIM and ASH oscillatory activity is larger than the AWA signal, and decreases over time. However, the magnitude of this oscillatory activity in RIM and ASH is higher in wild-type worms than in tyra-2 null-mutant worms **(Figure 5D, S4B, S4C)**. Furthermore, in virtual tyra-2 null-mutant worms, the magnitude of RIM and ASH activity decreases over the course of the simulation until it matches AWA activity, which permits exiting of the ring. After exiting, the AWA signal dominates, ASH becomes silent, and RIM becomes inhibited as the worm continuously ascends the diacetyl gradient (**Figure 5D**). The model thus predicts that RIM activity engages the RIM-ASH feedback loop, thereby decreasing threat tolerance and preventing exiting of the ring (**Figure 5D**). Importantly, the model also requires a non-linear threshold for RIM activation to trigger tyramine signaling to ASH and slow kinetics of accumulation and decay of the tyramine signal on a timescale of minutes to preclude exiting of wild-type worms even as the fructose barrier continues to diffuse and weaken (**Figure 5D, S4D**). The reduced activation of ASH and RIM in simulated tyra-2 null-mutant worms, in which tyraminergic RIM-ASH feedback is absent, encodes increased threat tolerance underlying increased propensity to exit the ring (**Figure 5D**). Our computational model thus suggests that the slow, continuous, and self-reinforcing enhancement of RIM and ASH activity by top-down tyraminergic positive feedback determines threat tolerance that ultimately controls the decision balance.

RIM-ASH positive feedback underlies modulation of the threat-reward decision by internal hunger state

Food deprivation increases threat tolerance in the multisensory decision paradigm (**Figure 1D**). We hypothesized it does so by suppressing RIM activity and thus the RIM-ASH tyraminergic feedback pathway. As a first test of this hypothesis, we examined the effect of food deprivation on tyra-2 null-mutant worms. In contrast to wild-type worms, tyra-2 null-mutant worms fail to increase exiting after one hour of food deprivation, and rather maintain their already elevated threat tolerance (**Figure 6A**). This is consistent with the hypothesis that one hour of food deprivation increases threat tolerance by suppressing tyraminergic RIM-ASH feedback, with tyra-2 null-mutant worms failing to increase exiting because the RIM-ASH pathway is already fully suppressed. We also measured the effects of food deprivation on unisensory osmotic avoidance. We found that tyra-2 null-mutant worms deprived of food for one hour exit more readily in the unisensory context, while wild-type worms are still retained (**Figure 6B**). This result also supports our model that food deprivation suppresses RIM activity and thus tyraminergic RIM-ASH feedback. In our model, RIM inhibition induced by food deprivation disinhibits forward command interneurons and reduces activation of backward command interneurons. This renders retreat from the osmotic ring reliant upon RIM-ASH positive feedback in this context. Five hours of food deprivation further increases exiting of tyra-2 null-mutant worms in the multisensory context, as seen in wild-type worms (**Figure 6A**). In the unisensory context, five hours of food deprivation further also increases exiting of both wild-type and tyra-2 null-mutant worms (**Figure 6B**). These effects of more extended food deprivation on tyra-2 null-mutant worms indicate the involvement of RIM-ASH-independent pathways for hunger-dependent increases in threat tolerance. Next we measured the effects of food deprivation

on unisensory attraction to food odor. We found that both wild-type and tyra-2 null-mutant worms exhibit enhanced chemotaxis to diacetyl after one or five hours of food deprivation (**Figure 6C, S5**). While increased chemotaxis to diacetyl in hungry wild-type and tyra-2 null-mutant worms could be driven by increased diacetyl sensitivity (Ryan et al., 2014), it is more likely that food deprivation increases attraction to diacetyl by effects on locomotion that result from suppressed RIM activity (Gordus et al., 2015; Gray et al., 2005).

To further test the hypothesis that food deprivation inhibits RIM, we turned to our computational model. We simulated food deprivation as duration-dependent tonic inhibition of RIM, keeping all other model parameters unchanged. We modeled one hour of food deprivation as RIM inhibition of ~0.03 (in arbitrary units), because this level of RIM inhibition increases exiting of simulated wild-type worms to 50%, the same as real worms food-deprived for one hour (compare **Figure 6A** with **Figure 6D**). As RIM inhibition increases from 0 to ~0.03, simulated wild-type worms increase exiting more steeply than tyra-2 null-mutant worms (**Figure 6D, S4E, S4F,** see **Supplemental Movie 1**). This qualitatively recapitulates the multisensory experimental results (**Figure 6A**). In the unisensory fructose-only context, as RIM inhibition increases from 0 to ~0.03, simulated wild-type worms increase exiting less steeply than tyra-2 null-mutant worms (**Figure 6E**). This qualitatively recapitulates the unisensory experimental results (**Figure 6B**). We note that model parameters were selected solely to match simulated exiting rates (**Figure 5B**) to experimental exiting rates of non-food-deprived worms (**Figure 2B**), without any consideration of the effects of food deprivation. Nonetheless, the qualitative recapitulation of experimental effects of increasing food deprivation in both unisensory and multisensory contexts by simulating increasing inhibition of RIM strongly reinforce the

conclusion that food deprivation increases threat tolerance by inhibiting RIM and thereby suppressing RIM-ASH tyraminergic feedback.

Tyramine supplementation and direct inhibition of RIM each recapitulate hunger state modulation of the threat-reward decision via RIM-ASH positive feedback

The results presented thus far support a model in which food deprivation increases threat tolerance by inhibiting RIM and thereby suppressing RIM-ASH tyraminergic feedback. To provide additional experimental tests of this model, we directly manipulated neural activity within the circuit. To exogenously induce tyraminergic potentiation of ASH, we added tyramine to the assay plate. Our model predicts that exogenous tyramine will increase threat sensitivity and thereby promote retreat from the ring in multisensory contexts via tyra-2 (**Figure 7A**). Exogenous tyramine has no effect on wild-type worms, which already exhibit maximum threat sensitivity (**Figure 7B**). In contrast, exogenous tyramine suppresses exiting of tdc-1 null-mutant worms exiting to wild-type levels (**Figure 7B**). Importantly, the effect of exogenous tyramine is completely eliminated in tyra-2 null-mutant worms (**Figure 7B**). We next tested the effect of exogenous tyramine on wild-type worms food-deprived for one hour. Our model predicts that one-hour food deprivation increases exiting via suppression of RIM-ASH tyraminergic feedback; therefore, the presence of tyramine, regardless of the worm's internal state, should suppress exiting. Indeed, wild-type worms food-deprived for one hour behave like sated worms in the presence of exogenous tyramine (**Figure 7C**). Again, tyra-2 null-mutant worms are unaffected (**Figure 7C**). Tyramine supplementation completely reverses increased exiting of one-hour food-deprived wild-type worms, thus further indicating that suppression of RIM-ASH tyraminergic feedback underlies increased threat tolerance of hungry worms.

Complementarily, our model predicts that direct inhibition of RIM activity should increase exiting (**Figure 7D**). Transgenic expression of a histamine-gated chloride channel (His-Cl) specifically in RIM allows for controlled silencing of RIM contingent upon the presence of exogenously applied histamine, as worms do not endogenously use histamine as a neurotransmitter (Pokala et al., 2014). In the absence of exogenous histamine, worms expressing His-Cl in RIM behave like wild-type worms and fail to exit the ring (**Figure 7E**). Direct inhibition of RIM by addition of 10 mM histamine to the assay plate increases exiting to ~50%, identical to the behavior of tdc-1 and tyra-2 null-mutant worms (**Figure 7E**). Inhibition of RIM by addition of 30 mM histamine to the plate did not increase exiting any further (**Figure 7E**). Therefore while the absolute level to which RIM is inhibited by histamine is unknown, activation of His-Cl and histamine-mediated inhibition of RIM are apparently saturated by 10 mM histamine. Our model predicts that one hour of food deprivation increases exiting by inhibiting RIM activity; therefore, as with tyra-2 null-mutant worms, no further increase in exiting of hungry worms is predicted when RIM is directly inhibited. In the absence of histamine, like wild-type worms, worms expressing His-Cl in RIM increase exiting after one hour of food-deprivation (**Figure 7F**). As predicted by our model, direct inhibition of RIM with histamine has no further effect on exiting of these one-hour food-deprived worms (**Figure 7F**). Taken together, these effects of exogenous tyramine and direct inhibition of RIM demonstrate that suppression of RIM-ASH tyraminergic feedback through RIM inhibition quantitatively accounts for the entirety of increased threat tolerance induced by one hour of food deprivation.

DISCUSSION

Here we demonstrate that tyraminergic RIM-ASH positive feedback controls multisensory threat-reward decision making in C. elegans. PDFR-1 activation by PDF-2 in RIM (**Figure 2, 3**) and extrasynaptic tyraminergic potentiation of ASH (**Figure 4**) set the decision balance between retreat from an osmotic threat and approach to food odor. We devised a minimal computational neural network model to recapitulate the decision in silico. Our model predicts that integration of multisensory inputs in RIM nonlinearly determines the magnitude of the tyramine feedback signal. Using this model, we simulated the dynamic changes in neural and neuromodulatory activity that occur in freely moving worms during decision making, and determined the slow timescale at which RIM-ASH tyraminergic feedback must act to implement the decision (**Figure 5, S4D**). Our experimental and computational results establish that food deprivation increases threat tolerance through suppression of RIM-ASH positive feedback by inhibition of RIM (**Figures 6, 7, S4E, S4F**). These studies provide an integrated neuroendocrine circuit architecture for internal state control of multisensory threat-reward decision making.

Tyramine secreted by RIM regulates multisensory decision making by modulating ASH sensitivity extrasynaptically at a distance. Interestingly, our modeling studies predict that the extrasynaptic tyramine signal must both accumulate and decay slowly, modulating ASH sensitivity over long time-scales of multiple minutes in order to appropriately implement the threat-reward decision balance. The computational model is agnostic as to how the slow kinetics of tyramine signaling are implemented. We propose that this slow tyramine signaling functions as a form of memory for the worm by suppressing sensory adaptation to dangerous stimuli sensed over time, a feature which could be advantageous for worms navigating changing environmental conditions. Slow-acting diffusion and accumulation of extrasynaptic signals that

act at a distance like tyramine are likely better suited for this purpose than more fast-acting synaptic signals. In addition, tyraminergic RIM-ASH positive feedback could determine the worm's tolerance to a variety of threats, as the ASH neuron is polymodal and senses multiple noxious cues (Hilliard et al., 2005; Kaplan and Horvitz, 1993).

We conclusively demonstrate that suppression of RIM-ASH tyraminergic feedback through RIM inhibition quantitatively accounts for the entirety of increased threat tolerance induced by one hour of food deprivation. Our studies indicate that RIM is a metabolic modulator of threat-reward decision making. Interestingly, we found that the direct synaptic connections that RIM forms with downstream command locomotor interneurons driving basic attraction and aversion behaviors are dispensable for modulation of threat-reward decision-making. In the decision studied here, the only function of RIM is to provide tyraminergic feedback to ASH based on metabolic state. Extended food deprivation beyond one hour then recruits other currently unknown RIM-ASH-independent pathways for hunger-dependent increases in threat tolerance. It was recently shown that in RIM and RIC, expression of NKAT-1, an enzyme in the biosynthetic pathway of kynurenic acid, a metabolite whose levels vary with hunger state, underlies hunger modulation of feeding rate (Lemieux et al., 2015). This provides a potential cellular mechanism linking organismic metabolic state to RIM excitability, thereby controlling tyramine secretion, and thus determines the likelihood of exiting the ring during the decision task.

Cell-specific rescue and t-PDF-2 expression experiments support the existence of a PDF-2-PDFR-1 autocrine loop in RIM. Interestingly, autocrine PDF signaling also occurs in the Drosophila circadian control network (Choi et al., 2012). Activation of autocrine positive feedback loops, however, are probably not easily reversible – therefore, it is likely that these

cascades are only initiated beyond a threshold level of activation modulated by externally derived signals or internal cellular state. Such a mechanism would reinforce the stability of distinct, long-lasting behavioral states, such as behaviors relevant to night versus day, or, in this case, biasing threat-reward decision making in the threat-tolerant or threat-sensitive directions. Therefore, we propose that by flipping a potentially stable switch, the PDF-2-PDFR-1 autocrine loop biases the worm towards threat-sensitive decisions and importantly, eliminates ambivalence when confronted with various situations.

How does RIM-ASH positive feedback control threat-reward decision making? The worm sensory interneuron network downstream of primary sensory neurons captures multisensory information (Ishihara et al., 2002; Luo et al., 2014; Shinkai et al., 2011), and RIM is downstream of this network (Gordus et al., 2015; Guo et al., 2009; Piggott et al., 2011; White et al., 1986). Thus we propose that RIM excitability is set by PDF-2-PDFR-1 autocrine loop activity, and RIM activity fluctuates dynamically as it responds to specific combinations of diacetyl and osmotic stimuli as the worm navigates the decision arena. Ultimately, the worm makes a probabilistic choice between retreat and exit based on the stochastic, instantaneous activity state of RIM, with stochasticity of RIM activity having been previously observed (Gordus et al., 2015). Longer time-scale tyraminergic feedback increases the probability that instantaneous RIM, and therefore ASH, activity states are high. Thus by acutely modifying forward and backward locomotor-control neuron activity through feedforward channels or, on longer time scales, indirectly through tyraminergic RIM-ASH feedback, RIM activity transforms multisensory inputs into a motor decision (**Figure S6**).

As discussed previously, in human beings and other mammals, a key feature of multisensory integration is internal-state-dependent “top-down” control of perception (Manita et

al., 2015; Talsma et al., 2010) by higher-order brain regions (Fairhall and Macaluso, 2009; Fu et al., 2014; Zhang et al., 2014). Interestingly, in the human brain, aminergic neuromodulatory systems like locus ceoruleus are involved in directing attention to food-related cues in a hunger-dependent manner (Mohanty et al., 2008). However, analysis of neural mechanisms in the context of an approach-avoidance decision in human and mammalian systems are limited by technical constraints. Here we describe an integrated circuit that demonstrates a mechanism by which internal physiological hunger state drives a shift in the decision balance of approach and avoidance. The molecular, cellular, and network motifs described here in the worm may be relevant in more complex nervous systems.

EXPERIMENTAL PROCEDURES

All C. elegans strains were maintained on Nematode Growth Medium (NGM) agar plates with E. coli OP50 as a food source. Transgenic strains were constructed by injection of plasmid DNA into the germline using standard methods. At least three independent lines were generated, tested, and results aggregated for each transgene.

Behavioral assays

For unisensory and multisensory assays, 10µL of fructose solution is applied in a 1cm diameter ring centered on a standard NGM plate (Culotti and Russell, 1978). For multisensory assays, 1µL diluted diacetyl was applied to each side of the plate, at least 1cm from the ring border. Ten (unless otherwise indicated) adult worms were transferred inside the ring. Fifteen minutes later, the number of worms outside the ring were counted. For the food deprivation assays, worms were transferred inside the ring from another plate, where they were kept without food for the indicated time interval. For this and other assays, see **Supplemental Experimental Procedures** for more information. At least five independent assays were performed for each condition. One- or two-way ANOVA, as appropriate, was used to analyze statistical differences, with post-hoc Tukey-Kramer tests performed for pairwise comparisons between all pairs of genotypes. We did not include all previously tested genotypes/conditions each time a new genotype/condition was tested. Therefore identical data was presented in multiple figure panels.

Imaging

Calcium imaging of ASH neurons was performed on young adult worms immobilized in an olfactory chamber as described previously (Chronis et al., 2007). Imaged animals expressed

the genetically-encoded calcium sensor GCaMP3 from the sra-6 promoter (Tian et al., 2009). Prior to loading into the olfactory chamber worms were bathed in neuronal buffer for 10 min either in the presence or absence of 50mM tyramine. Animals were exposed to the test stimulus for 20 sec. Averaged fluorescence was calculated for a region of interest (ROI) surrounding the ASH soma. The percent change in fluorescence for each frame was calculated relative to the corrected fluorescence of the ROI just prior to stimulus onset. See **Supplemental Experimental Procedures** for more details.

Computational model

Model animals possess a simplified nervous system comprising sensory neurons AWA and ASH, interneuron RIM, and two reciprocally inhibited motor neurons denoted DMN and VMN, which activate dorsal and ventral body bends, respectively. AWA and ASH sensory neurons respond with transient activation to changes in diacetyl or fructose stimuli, respectively. Activation of model sensory neurons AWA and ASH provides differentially weighted inhibitory and excitatory inputs onto RIM, respectively. RIM integrates these sensory inputs and inhibits motorneurons DMN and VMN to bias dorsal versus ventral bends, thereby inducing gradual steering of the worm. Additionally, RIM activity positively increases the likelihood of pirouettes, which are modeled as instantaneous step changes in angular heading. The simulation also includes RIM-ASH tyraminergic positive feedback. Tyraminergic potentiation of ASH in the model is only engaged above a threshold level of RIM activation. tyra-2 null-mutant worms are modeled as lacking this tyraminergic feedback to ASH. Model parameters were manually calibrated until exiting rates of simulated wild-type and tyra-2 null-mutant worms matched experimental exiting rates in multisensory and unisensory contexts for 2 M, 3 M, and 4 M fructose. The virtual decision arena comprises a continuously diffusing fructose gradient ring and

time-invariant diacetyl gradients originating from two spots outside the ring. Each simulation begins with a single worm in the center of the virtual arena with a randomly selected initial heading, and the simulation is allowed to proceed for fifteen virtual minutes. See **Supplemental Experimental Procedures** for additional details.

Author Contributions

DDG, TS, NC, MRK, MNN designed study and experiments. DDG, SH, DLC performed experiments. TS and NC performed computational modeling. DDG, TS, LYM, DLC, NC, MRK, and MNN analyzed the data. DDG and MNN wrote the paper with input from the other authors.

Author Information

The authors declare no conflicts of interest.

Correspondence and requests for material should be addressed to michael.nitabach@yale.edu.

Acknowledgments

We thank S. Mitani, C. Bargmann, and the Caenorhabditis Genetics Center for strains, K. Ashrafi, A. Maricq, C. Rankin, D. Colon-Ramos, M. Chalfie for cell-specific promoter reagents, M. Hammarlund for other vectors, V. Reinke for assistance and advice, G. Jansen for sharing unpublished data, assistance and advice in generating the computational model, S. Braunstein, members of the Cohen, Koelle, and Nitabach labs and the Yale worm community for technical advice and comments, and Daeyeol Lee and Leslie Vosshall for comments on the manuscript. D.D.G was supported by a National Institute of Neurological Disease and Stroke (NINDS) National Institutes of Health (NIH) Predoctoral Fellowship (F31NS080628). Work in the laboratory of M.N.N. was supported in part by NINDS, NIH (R01NS055035, R01NS056443, R01NS091070) and National Institute of General Medical Sciences, NIH (R01GM098931). M.R.K. was supported by NINDS, NIH (R01NS036918). N.C. and T.S. were supported by the Engineering and Physical Sciences Research Council (EPSRC, EP/J004057/1). Computational work was undertaken on ARC2 and MARC1 (High Performance Computing facilities, University of Leeds). MARC1 was funded by the Leeds Institute for Data Analytics.

References

Alkema, M.J., Hunter-Ensor, M., Ringstad, N., and Horvitz, H.R. (2005). Tyramine Functions independently of octopamine in the Caenorhabditis elegans nervous system. Neuron *46*, 247-260.

Barrios, A., Ghosh, R., Fang, C., Emmons, S.W., and Barr, M.M. (2012). PDF-1 neuropeptide signaling modulates a neural circuit for mate-searching behavior in C. elegans. Nature neuroscience *15*, 1675-1682.

Berthoud, H.R. (2011). Metabolic and hedonic drives in the neural control of appetite: who is the boss? Curr Opin Neurobiol *21*, 888-896.

Choi, C., Cao, G., Tanenhaus, A.K., McCarthy, E.V., Jung, M., Schleyer, W., Shang, Y., Rosbash, M., Yin, J.C., and Nitabach, M.N. (2012). Autoreceptor control of peptide/neurotransmitter corelease from PDF neurons determines allocation of circadian activity in drosophila. Cell Rep *2*, 332-344.

Choi, C., Fortin, J.P., McCarthy, E., Oksman, L., Kopin, A.S., and Nitabach, M.N. (2009). Cellular dissection of circadian peptide signals with genetically encoded membrane-tethered ligands. Current biology : CB *19*, 1167-1175.

Choi, S., Chatzigeorgiou, M., Taylor, K.P., Schafer, W.R., and Kaplan, J.M. (2013). Analysis of NPR-1 reveals a circuit mechanism for behavioral quiescence in C. elegans. Neuron *78*, 869-880.

Chronis, N., Zimmer, M., and Bargmann, C.I. (2007). Microfluidics for in vivo imaging of neuronal and behavioral activity in Caenorhabditis elegans. Nature methods *4*, 727-731.

Cohen, N., and Sanders, T. (2014). Nematode locomotion: dissecting the neuronal-environmental loop. Curr Opin Neurobiol *25*, 99-106.

Culotti, J.G., and Russell, R.L. (1978). Osmotic avoidance defective mutants of the nematode Caenorhabditis elegans. Genetics *90*, 243-256.

Donnelly, J.L., Clark, C.M., Leifer, A.M., Pirri, J.K., Haburcak, M., Francis, M.M., Samuel, A.D., and Alkema, M.J. (2013). Monoaminergic orchestration of motor programs in a complex C. elegans behavior. PLoS biology 11, e1001529.

Fairhall, S.L., and Macaluso, E. (2009). Spatial attention can modulate audiovisual integration at multiple cortical and subcortical sites. Eur J Neurosci 29, 1247-1257.

Flavell, S.W., Pokala, N., Macosko, E.Z., Albrecht, D.R., Larsch, J., and Bargmann, C.I. (2013). Serotonin and the neuropeptide PDF initiate and extend opposing behavioral states in C. elegans. Cell 154, 1023-1035.

Fortin, J.P., Zhu, Y., Choi, C., Beinborn, M., Nitabach, M.N., and Kopin, A.S. (2009). Membrane-tethered ligands are effective probes for exploring class B1 G protein-coupled receptor function. Proceedings of the National Academy of Sciences of the United States of America 106, 8049-8054.

Frezal, L., and Felix, M.A. (2015). C. elegans outside the Petri dish. Elife 4.

Fu, Y., Tucciarone, J.M., Espinosa, J.S., Sheng, N., Darcy, D.P., Nicoll, R.A., Huang, Z.J., and Stryker, M.P. (2014). A cortical circuit for gain control by behavioral state. Cell 156, 1139-1152.

Gordus, A., Pokala, N., Levy, S., Flavell, S.W., and Bargmann, C.I. (2015). Feedback from network States generates variability in a probabilistic olfactory circuit. Cell 161, 215-227.

Gray, J.M., Hill, J.J., and Bargmann, C.I. (2005). A circuit for navigation in Caenorhabditis elegans. Proceedings of the National Academy of Sciences of the United States of America 102, 3184-3191.

Guo, Z.V., Hart, A.C., and Ramanathan, S. (2009). Optical interrogation of neural circuits in Caenorhabditis elegans. Nature methods 6, 891-896.

Hilliard, M.A., Apicella, A.J., Kerr, R., Suzuki, H., Bazzicalupo, P., and Schafer, W.R. (2005). In vivo imaging of C. elegans ASH neurons: cellular response and adaptation to chemical repellents. The EMBO journal 24, 63-72.

Ishihara, T., Iino, Y., Mohri, A., Mori, I., Gengyo-Ando, K., Mitani, S., and Katsura, I. (2002). HEN-1, a secretory protein with an LDL receptor motif, regulates sensory integration and learning in Caenorhabditis elegans. Cell 109, 639-649.

Janssen, T., Husson, S.J., Lindemans, M., Mertens, I., Rademakers, S., Ver Donck, K., Geysen, J., Jansen, G., and Schoofs, L. (2008). Functional characterization of three G protein-coupled receptors for pigment dispersing factors in Caenorhabditis elegans. The Journal of biological chemistry 283, 15241-15249.

Janssen, T., Husson, S.J., Meelkop, E., Temmerman, L., Lindemans, M., Verstraelen, K., Rademakers, S., Mertens, I., Nitabach, M., Jansen, G., et al. (2009). Discovery and characterization of a conserved pigment dispersing factor-like neuropeptide pathway in Caenorhabditis elegans. Journal of neurochemistry 111, 228-241.

Jin, X., Pokala, N., and Bargmann, C.I. (2016). Distinct Circuits for the Formation and Retrieval of an Imprinted Olfactory Memory. Cell 164, 632-643.

Jose, A.M., Bany, I.A., Chase, D.L., and Koelle, M.R. (2007). A specific subset of transient receptor potential vanilloid-type channel subunits in Caenorhabditis elegans endocrine cells function as mixed heteromers to promote neurotransmitter release. Genetics 175, 93-105.

Kaplan, J.M., and Horvitz, H.R. (1993). A dual mechanosensory and chemosensory neuron in Caenorhabditis elegans. Proceedings of the National Academy of Sciences of the United States of America 90, 2227-2231.

Kawano, T., Po, M.D., Gao, S., Leung, G., Ryu, W.S., and Zhen, M. (2011). An imbalancing act: gap junctions reduce the backward motor circuit activity to bias C. elegans for forward locomotion. Neuron 72, 572-586.

Krupp, J.J., Billeter, J.C., Wong, A., Choi, C., Nitabach, M.N., and Levine, J.D. (2013). Pigment-dispersing factor modulates pheromone production in clock cells that influence mating in drosophila. Neuron 79, 54-68.

Kunst, M., Hughes, M.E., Raccuglia, D., Felix, M., Li, M., Barnett, G., Duah, J., and Nitabach, M.N. (2014). Calcitonin gene-related peptide neurons mediate sleep-specific circadian output in Drosophila. Current biology : CB 24, 2652-2664.

Lemieux, G.A., Cunningham, K.A., Lin, L., Mayer, F., Werb, Z., and Ashrafi, K. (2015). Kynurenic acid is a nutritional cue that enables behavioral plasticity. Cell 160, 119-131.

Li, Z., Li, Y., Yi, Y., Huang, W., Yang, S., Niu, W., Zhang, L., Xu, Z., Qu, A., Wu, Z., et al. (2012). Dissecting a central flip-flop circuit that integrates contradictory sensory cues in C. elegans feeding regulation. Nat Commun 3, 776.

Luo, L., Wen, Q., Ren, J., Hendricks, M., Gershow, M., Qin, Y., Greenwood, J., Soucy, E.R., Klein, M., Smith-Parker, H.K., et al. (2014). Dynamic encoding of perception, memory, and movement in a C. elegans chemotaxis circuit. Neuron 82, 1115-1128.

Manita, S., Suzuki, T., Homma, C., Matsumoto, T., Odagawa, M., Yamada, K., Ota, K., Matsubara, C., Inutsuka, A., Sato, M., et al. (2015). A Top-Down Cortical Circuit for Accurate Sensory Perception. Neuron.

Meelkop, E., Temmerman, L., Janssen, T., Suetens, N., Beets, I., Van Rompay, L., Shanmugam, N., Husson, S.J., and Schoofs, L. (2012). PDF receptor signaling in Caenorhabditis

elegans modulates locomotion and egg-laying. Molecular and cellular endocrinology 361, 232-240.

Mohanty, A., Gitelman, D.R., Small, D.M., and Mesulam, M.M. (2008). The spatial attention network interacts with limbic and monoaminergic systems to modulate motivation-induced attention shifts. Cereb Cortex 18, 2604-2613.

Piggott, B.J., Liu, J., Feng, Z., Wescott, S.A., and Xu, X.Z. (2011). The neural circuits and synaptic mechanisms underlying motor initiation in C. elegans. Cell 147, 922-933.

Pirri, J.K., McPherson, A.D., Donnelly, J.L., Francis, M.M., and Alkema, M.J. (2009). A tyramine-gated chloride channel coordinates distinct motor programs of a Caenorhabditis elegans escape response. Neuron 62, 526-538.

Pokala, N., Liu, Q., Gordus, A., and Bargmann, C.I. (2014). Inducible and titratable silencing of Caenorhabditis elegans neurons in vivo with histamine-gated chloride channels. Proceedings of the National Academy of Sciences of the United States of America 111, 2770-2775.

Rangel, A., Camerer, C., and Montague, P.R. (2008). A framework for studying the neurobiology of value-based decision making. Nat Rev Neurosci 9, 545-556.

Rex, E., Hapiak, V., Hobson, R., Smith, K., Xiao, H., and Komuniecki, R. (2005). TYRA-2 (F01E11.5): a Caenorhabditis elegans tyramine receptor expressed in the MC and NSM pharyngeal neurons. Journal of neurochemistry 94, 181-191.

Rex, E., and Komuniecki, R.W. (2002). Characterization of a tyramine receptor from Caenorhabditis elegans. Journal of neurochemistry 82, 1352-1359.

Rex, E., Molitor, S.C., Hapiak, V., Xiao, H., Henderson, M., and Komuniecki, R. (2004). Tyramine receptor (SER-2) isoforms are involved in the regulation of pharyngeal

pumping and foraging behavior in Caenorhabditis elegans. Journal of neurochemistry 91, 1104-1115.

Ryan, D.A., Miller, R.M., Lee, K., Neal, S.J., Fagan, K.A., Sengupta, P., and Portman, D.S. (2014). Sex, age, and hunger regulate behavioral prioritization through dynamic modulation of chemoreceptor expression. Current biology : CB 24, 2509-2517.

Sengupta, P., Chou, J.H., and Bargmann, C.I. (1996). odr-10 encodes a seven transmembrane domain olfactory receptor required for responses to the odorant diacetyl. Cell 84, 899-909.

Shinkai, Y., Yamamoto, Y., Fujiwara, M., Tabata, T., Murayama, T., Hirotsu, T., Ikeda, D.D., Tsunozaki, M., Iino, Y., Bargmann, C.I., et al. (2011). Behavioral choice between conflicting alternatives is regulated by a receptor guanylyl cyclase, GCY-28, and a receptor tyrosine kinase, SCD-2, in AIA interneurons of Caenorhabditis elegans. The Journal of neuroscience : the official journal of the Society for Neuroscience 31, 3007-3015.

Solomon, A., Bandhakavi, S., Jabbar, S., Shah, R., Beitel, G.J., and Morimoto, R.I. (2004). Caenorhabditis elegans OSR-1 regulates behavioral and physiological responses to hyperosmotic environments. Genetics 167, 161-170.

Talsma, D. (2015). Predictive coding and multisensory integration: an attentional account of the multisensory mind. Front Integr Neurosci 9, 19.

Talsma, D., Senkowski, D., Soto-Faraco, S., and Woldorff, M.G. (2010). The multifaceted interplay between attention and multisensory integration. Trends in cognitive sciences 14, 400-410.

Tian, L., Hires, S.A., Mao, T., Huber, D., Chiappe, M.E., Chalasani, S.H., Petreanu, L., Akerboom, J., McKinney, S.A., Schreiter, E.R., et al. (2009). Imaging neural activity in worms, flies and mice with improved GCaMP calcium indicators. Nature methods 6, 875-881.

Varshney, L.R., Chen, B.L., Paniagua, E., Hall, D.H., and Chklovskii, D.B. (2011). Structural properties of the Caenorhabditis elegans neuronal network. PLoS Comput Biol 7, e1001066.

Wang, D., Yu, Y., Li, Y., Wang, Y., and Wang, D. (2014). Dopamine receptors antagonistically regulate behavioral choice between conflicting alternatives in C. elegans. PLoS One 9, e115985.

White, J.G., Southgate, E., Thomson, J.N., and Brenner, S. (1986). The structure of the nervous system of the nematode Caenorhabditis elegans. Philosophical transactions of the Royal Society of London Series B, Biological sciences 314, 1-340.

Wragg, R.T., Hapiak, V., Miller, S.B., Harris, G.P., Gray, J., Komuniecki, P.R., and Komuniecki, R.W. (2007). Tyramine and octopamine independently inhibit serotonin-stimulated aversive behaviors in Caenorhabditis elegans through two novel amine receptors. The Journal of neuroscience : the official journal of the Society for Neuroscience 27, 13402-13412.

Zahratka, J.A., Williams, P.D., Summers, P.J., Komuniecki, R.W., and Bamber, B.A. (2015). Serotonin differentially modulates Ca2+ transients and depolarization in a C. elegans nociceptor. J Neurophysiol 113, 1041-1050.

Zhang, S., Xu, M., Kamigaki, T., Hoang Do, J.P., Chang, W.C., Jenvay, S., Miyamichi, K., Luo, L., and Dan, Y. (2014). Selective attention. Long-range and local circuits for top-down modulation of visual cortex processing. Science 345, 660-665.

Figure 1. Hunger state modulates a multisensory threat-reward decision

(A) Schematic of information flow in the C. elegans sensorimotor control network. The AWA primary sensory neuron that responds to attractive stimuli like diacetyl food odor indirectly inhibits the RIM interneuron. The ASH primary sensory neuron that responds to aversive stimuli like hyperosmolarity indirectly excites RIM. RIM directly inhibits forward command interneurons and directly excites backward command interneurons to control the balance between forward and backward locomotion. ASH also bypasses RIM to directly excite backward command interneurons.

(B) Schematic of the decision making assay. Worms (black squiggles) are placed in the center of a hyperosmotic fructose ring (red circle) with the food odor diacetyl (yellow spots) outside the ring. As each worm ascends the attractive diacetyl gradient, it encounters the aversive hyperosmotic ring, where it either proceeds to exit or retreats to remain in the ring. The decision balance is quantified as the percent of worms that exit the ring during a fifteen minute trial.

(C) Wild-type and odr-10 null-mutant worm tolerance of 2 M fructose ring in presence or absence of food odor. odr-10 null-mutant worms lack the olfactory receptor that senses diacetyl.

(D) Effect of increasing food deprivation on decision to exit a 3 M fructose ring in the presence of food odor.

(Identical data is presented in multiple data sets, as all previously tested genotypes/conditions were not tested every time we extended our analysis to additional genotypes/conditions. Unless otherwise indicated, data in all Figures represent the average of at least five independent assays with ten worms per assay. All statistical comparisons are by one- or two-way ANOVA, as

appropriate, with Tukey-Kramer paired-comparison test applied to all pairs of genotypes. Error bars denote s.e.m.; ***, $p \leq 0.001$.)

Figure 2. PDF-2 neuropeptide regulates multisensory decision making

(A) RIM is potentially a peptide-modulated locus for internal state control of threat-reward decision making. RIM expresses both the neuropeptide PDF-2 and its G protein-coupled receptor PDFR-1.

(B) Decision balance of wild-type and pdf-2 null-mutant worms encountering a 2 M, 3 M, or 4 M fructose ring in the presence or absence of food odor. Rescue of pdf-2 null-mutant phenotype by re-expression of a pdf-2 transgene under the control of its own promoter.

(C) Exiting of the osmotic ring in the absence of food odor in wild-type and pdf-2 null-mutant worms.

(D) Chemotaxis to various concentrations of diacetyl, measured as the fraction of worms that move to a test spot of diacetyl dilution versus a control spot of water after a fifteen minute trial on a standard assay plate, in wild-type and pdf-2 null-mutant worms.

(E) Representative five minute trajectories of wild-type and pdf-2 null-mutant worms inside a 3 M ring with food odor outside. The outer red circle represents the osmotic ring, and the shading indicates 1mm annular zones.

(F) Time spent by wild-type and pdf-2 null-mutant worms in each of the radial zones (n=7-10 worms for each genotype, $F = 1.688$, $p = 0.160$).

Figure 3. PDF-2 signaling to PDFR-1 in RIM controls the multisensory decision balance by modulating tyramine secretion

(A) Re-expression of PDF-2 in RIM and RIC in pdf-2 null-mutant worms using the tdc-1 promoter.

(B) Membrane-tethered peptide (t-peptide) system. Bioactive peptides can be expressed as chimeric fusion proteins with N-terminal secretory signal sequences and C-terminal glycolipid anchor targeting signals. t-peptides are secreted, but remain covalently anchored to the plasma membrane, and thus only activate their cognate receptors cell-autonomously. Adapted from Choi et al., 2009.

(C) Expression in pdf-2 null-mutant worms of t-PDF-2 using either of two promoters whose activity overlaps only in RIM; expression of t-PDF-2 in RIC alone; or expression of sequence-scrambled t-SCR in RIM and RIC. The tdc-1, nmr-2, and tbh-1 promoters are used to drive expression in RIM and RIC; RIM, multiple AV neurons, and PVC; and RIC alone, respectively.

(D) Tyramine is synthesized from tyrosine by tyrosine decarboxylase (TDC), encoded by the tdc-1 gene expressed in RIM and RIC. Octopamine is synthesized from tyramine by tyramine-β-hydroxylase (TBH), encoded by the tbh-1 gene expressed in RIC.

(E) Multisensory and unisensory decision balance of tdc-1 null-mutant worms, which lack both tyramine and octopamine, and tbh-1 null-mutant worms, which lack only octopamine. Decision balance of pdf-2; tdc-1 double-mutant is also shown.

(F) Re-expression of tdc-1 in RIM and RIC, but not RIC alone, in tdc-1 null-mutant worms.

Figure 4. Tyramine acts on its receptor TYRA-2 in ASH osmosensory neuron to regulate the multisensory decision balance

(A) Multisensory and unisensory decision balance of tyramine receptor mutants. Tyramine GPCR ser-2 null-mutant worms exhibit increased exiting in both multisensory (p vs wild-type = 0.136) and unisensory contexts, though only the increased exiting in the unisensory context is statistically significant compared to wild-type (**, p = 0.009). Decision balance of the pdf-2; tyra-2 double-mutant is also shown.

(B) Re-expression of tyra-2 in tyra-2 null-mutant worms under the control of the sra-6 or gpa-13 promoters, whose activity overlaps solely in ASH. Re-expression of tyra-2 using the mec-17 promoter in touch receptor neurons (TRN), some of which also normally express tyra-2.

(C-E) Representative images (C), time course (D), and peak (E) Ca^{2+} responses of ASH to 180 mM fructose (unless otherwise indicated) in wild-type worms with or without 50 mM tyramine pre-treatment imaged using GCaMP3.

(F-H) Representative images (F), time course (G), and peak (H) Ca^{2+} responses of ASH to 180 mM fructose in tyra-2 null-mutant worms with or without 50 mM tyramine pre-treatment imaged using GCaMP3.

(Arrows indicate ASH cell body, magnified in the insets. Dashed lines outline the worm. mean $\pm$ s.e.m; circles represent peak responses of individual animals; n>12 animals per genotype and treatment condition.)

Figure 5. Computational modeling predicts non-linear slow tyramine signaling by RIM to ASH

(A) Schematic of the simplified nervous system used for computational modeling. AWA and ASH provide direct inhibitory and excitatory inputs onto RIM, respectively. RIM integrates these sensory inputs and directionally biases forward locomotion via inhibition of steering and pirouette modulation. Tyraminergic positive feedback from RIM to ASH increases ASH sensitivity to osmotic stimuli. Simulated tyra-2 null-mutant worms lack the tyraminergic RIM-ASH signal.

(B) Decision balance of simulated wild-type and tyra-2 null-mutant worms encountering a 2 M, 3 M, or 4 M fructose ring in the presence or absence of food odor. n=1000 single worm simulations per genotype and condition.

(C) Sample fifteen-minute trajectories of simulated wild-type and tyra-2 null-mutant worms inside a 3 M ring with food odor outside. Trajectories are magnified in the insets.

(D) Neural activity profiles of AWA, ASH, and RIM during the simulated trajectories in (**C**). Activity of individual neurons and of tyramine signals are expressed in arbitrary units, plotted to the same scale for the simulated wild-type and tyra-2 null-mutant worms.

Figure 6. One-hour food deprivation fails to increase threat tolerance of tyra-2 null-mutant worms

(A-C) Effect of one hour or five hours of food deprivation on wild-type and tyra-2 null-mutant worm multisensory decision balance (A), exiting of a 3 M fructose ring in the absence of food odor (B), and chemotaxis to 1:1000 diacetyl (C). (*, $p<0.05$.)

(D and **E)** Effect of increasing RIM inhibition on simulated wild-type and tyra-2 null-mutant worm multisensory (D) or unisensory (E) decision balance. Vertical dashed lines indicate the

degree of RIM inhibition that results in exiting rates for simulated wild-type worms that match those of real worms deprived of food for the indicated durations (see panel A). n=250 simulated worms for each genotype and strength of RIM inhibition.

Figure 7. One-hour food deprivation increases threat tolerance by inhibiting RIM activity and suppressing RIM-ASH tyraminergic potentiation

(A) Schematic depicting prediction that exogenous tyramine increases threat sensitivity. Exogenous tyramine is predicted to reverse the effects of suppression of the RIM-ASH positive feedback loop on threat sensitivity. Yellow represents strong activity, while blue represents weak activity. Thickness of solid lines represents strength of signals, and dashed lines represent inactive signals.

(B) Effect of exogenous tyramine on multisensory decisions of wild-type, tdc-1 null-mutant, and tyra-2 null-mutant worms.

(C) Effect of **e**xogenous tyramine on multisensory decisions of one-hour food-deprived wild-type and tyra-2 null-mutant worms.

(D) Schematic depicting prediction that inhibition of RIM increases threat tolerance. Inhibition of RIM expressing His-Cl with exogenous histamine is predicted to increase threat tolerance and mimic one hour of food deprivation.

(E) Effect of 0, 10 mM, and 30 mM histamine on multisensory decision balance of worms expressing RIM::His-Cl.

(F) Effect of 0 and 10 mM histamine on multisensory decision balance of one-hour food-deprived worms expressing RIM::His-Cl.

Figure 1

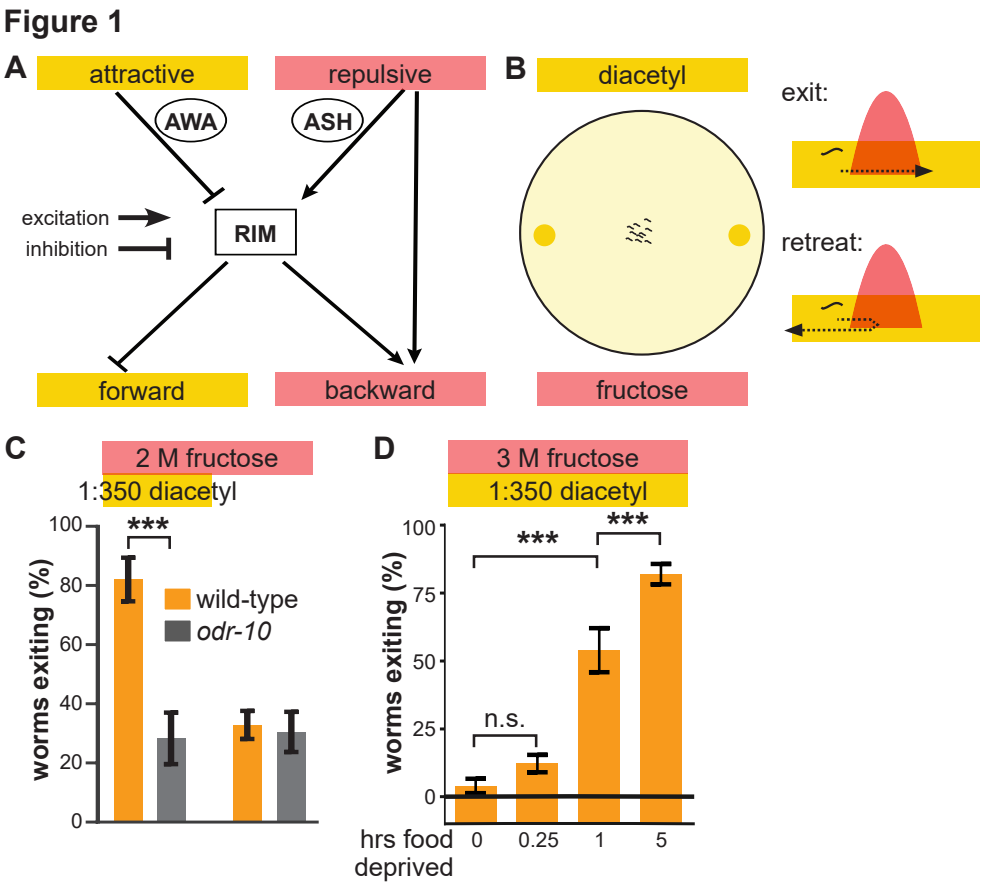
Figure 1
A
attractive
repulsive
AWA
ASH
excitation
inhibition
RIM
forward
backward
B
diacetyl
fructose
exit:
retreat:
C
2 M fructose
1:350 diacetyl
***
100
80
60
40
20
0
worms exiting (%)
wild-type
odr-10
D
3 M fructose
1:350 diacetyl
***
***
n.s.
100
75
50
25
0
worms exiting (%)
hrs food deprived
0
0.25
1
5

Figure 2

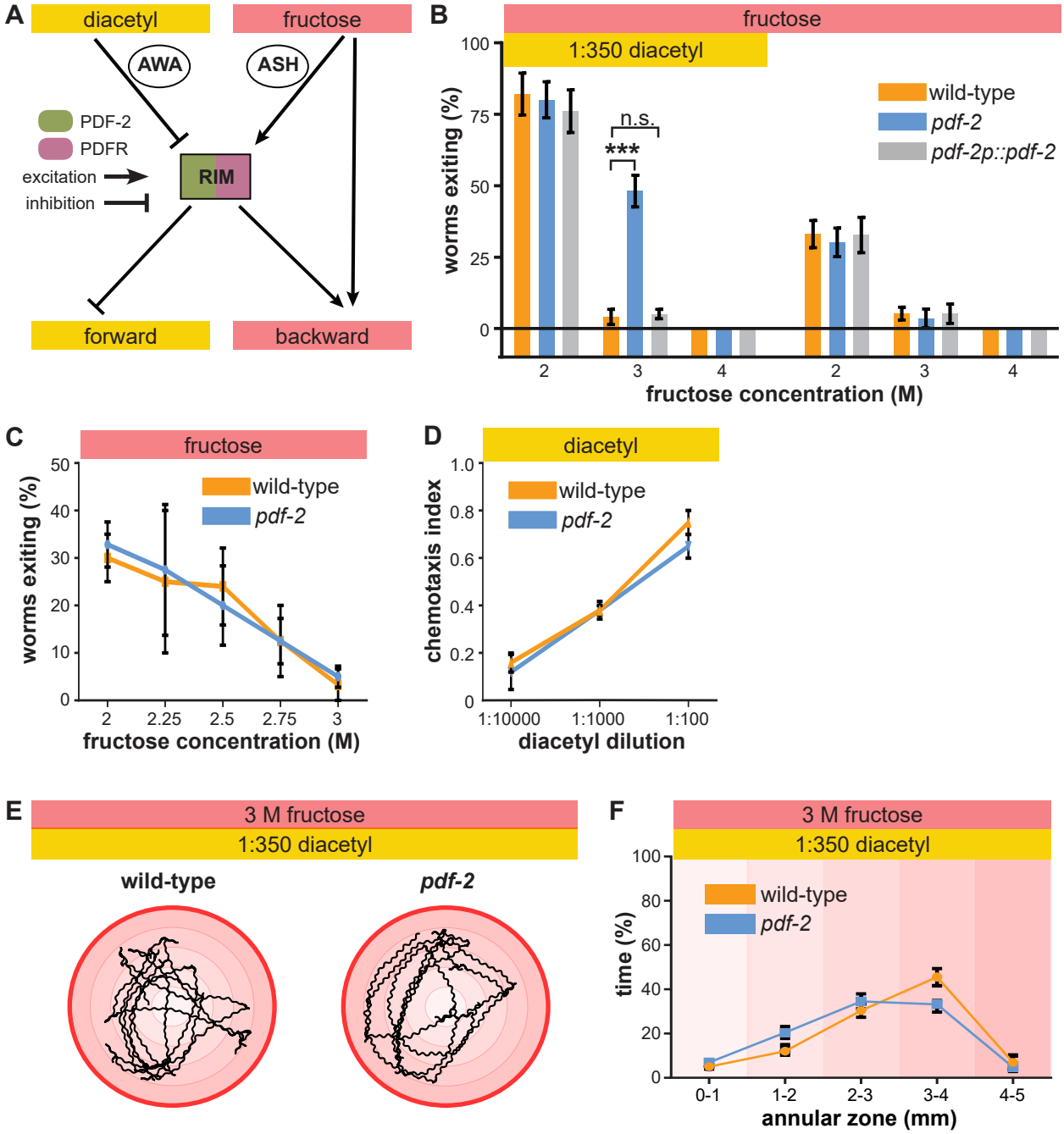
A
diacetyl
fructose
AWA
ASH
PDF-2
PDFR
excitation
inhibition
RIM
forward
backward
B
fructose
1:350 diacetyl
wild-type
pdf-2
pdf-2p::pdf-2
n.s.
***
worms exiting (%)
fructose concentration (M)
C
fructose
wild-type
pdf-2
worms exiting (%)
fructose concentration (M)
D
diacetyl
wild-type
pdf-2
chemotaxis index
diacetyl dilution
E
3 M fructose
1:350 diacetyl
wild-type
pdf-2
F
3 M fructose
1:350 diacetyl
wild-type
pdf-2
time (%)
annular zone (mm)

Figure 3

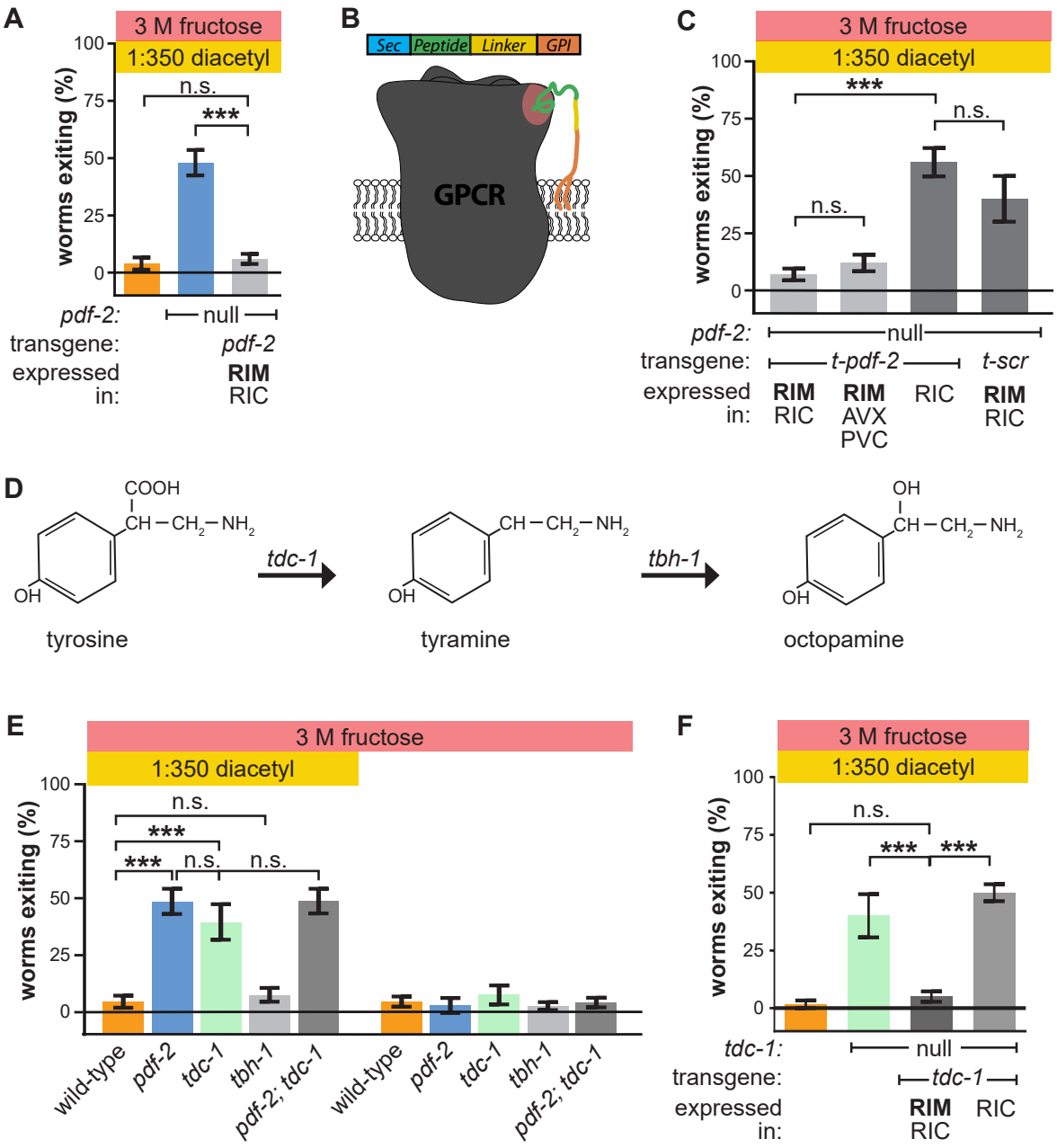
Figure 3
A
3 M fructose
1:350 diacetyl
worms exiting (%)
100
75
50
25
0
n.s.
***
pdf-2:
null
transgene:
pdf-2
expressed in:
RIM
RIC
B
Sec
Peptide
Linker
GPI
GPCR
C
3 M fructose
1:350 diacetyl
worms exiting (%)
***
n.s.
n.s.
pdf-2:
null
transgene:
t-pdf-2
t-scr
expressed in:
RIM
RIC
RIM
AVX
PVC
RIC
RIM
RIC
D
COOH
CH – CH2 – NH2
OH
tdc-1
tyrosine
tyramine
tbh-1
OH
octopamine
E
3 M fructose
1:350 diacetyl
worms exiting (%)
n.s.
***
***
n.s.
n.s.
wild-type
pdf-2
tdc-1
tbh-1
pdf-2; tdc-1
F
3 M fructose
1:350 diacetyl
worms exiting (%)
n.s.
***
***
tdc-1:
null
transgene:
tdc-1
expressed in:
RIM
RIC
RIC

Figure 4

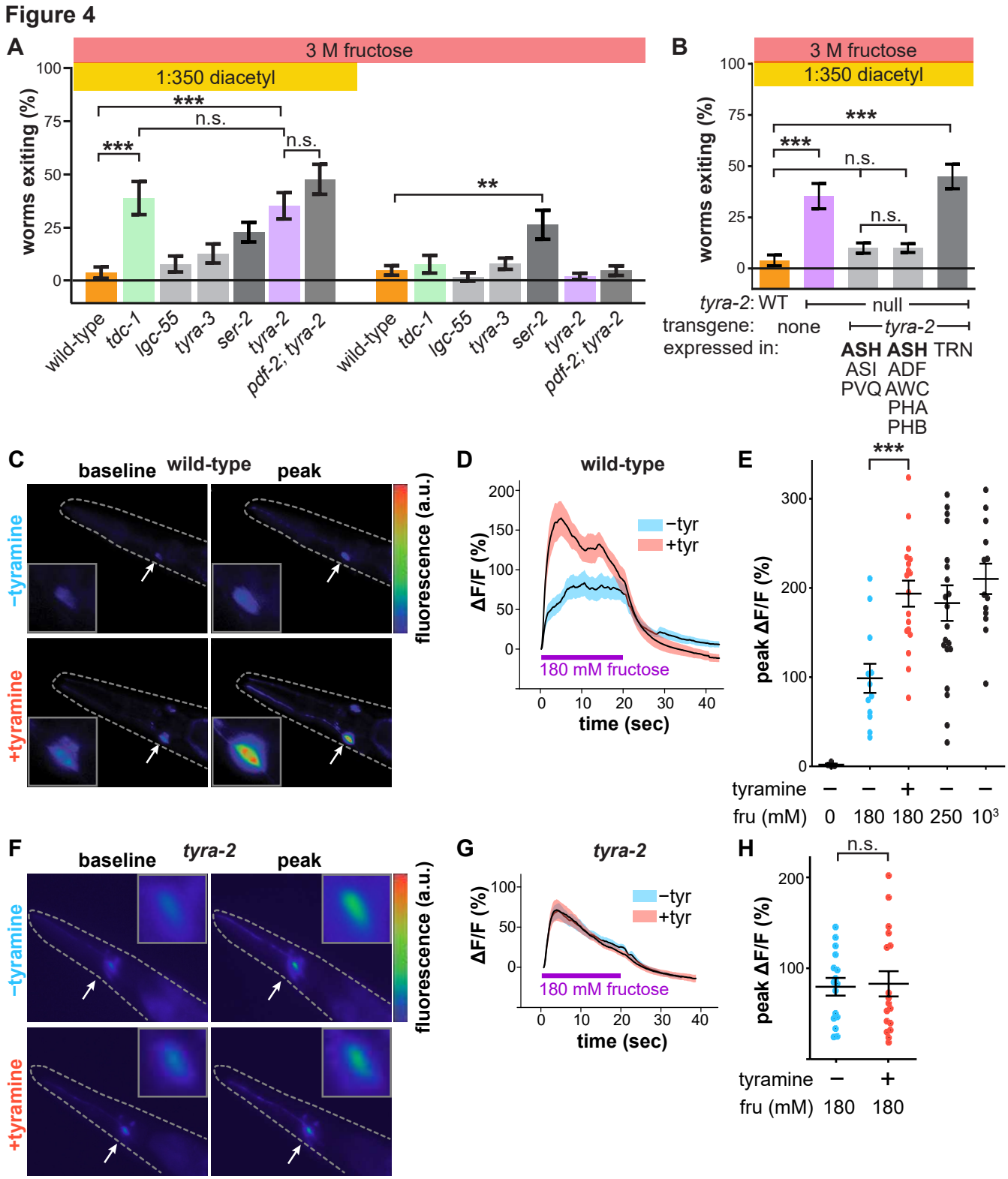
Figure 4
A
3 M fructose
1:350 diacetyl
worms exiting (%)
100
75
50
25
0
***
n.s.
***
n.s.
**
wild-type
tdc-1
lgc-55
tyra-3
ser-2
tyra-2
pdf-2; tyra-2
B
3 M fructose
1:350 diacetyl
worms exiting (%)
tyra-2: WT
null
transgene: none
tyra-2
expressed in:
ASH ASH TRN
ASI ADF
PVQ AWC
PHA
PHB
C
baseline
wild-type
peak
−tyramine
+tyramine
fluorescence (a.u.)
D
wild-type
ΔF/F (%)
−tyr
+tyr
180 mM fructose
time (sec)
E
peak ΔF/F (%)
tyramine
fru (mM) 0 180 180 250 10³
F
baseline
tyra-2
peak
−tyramine
+tyramine
fluorescence (a.u.)
G
tyra-2
ΔF/F (%)
−tyr
+tyr
180 mM fructose
time (sec)
H
n.s.
peak ΔF/F (%)
tyramine
fru (mM) 180 180

Figure 5

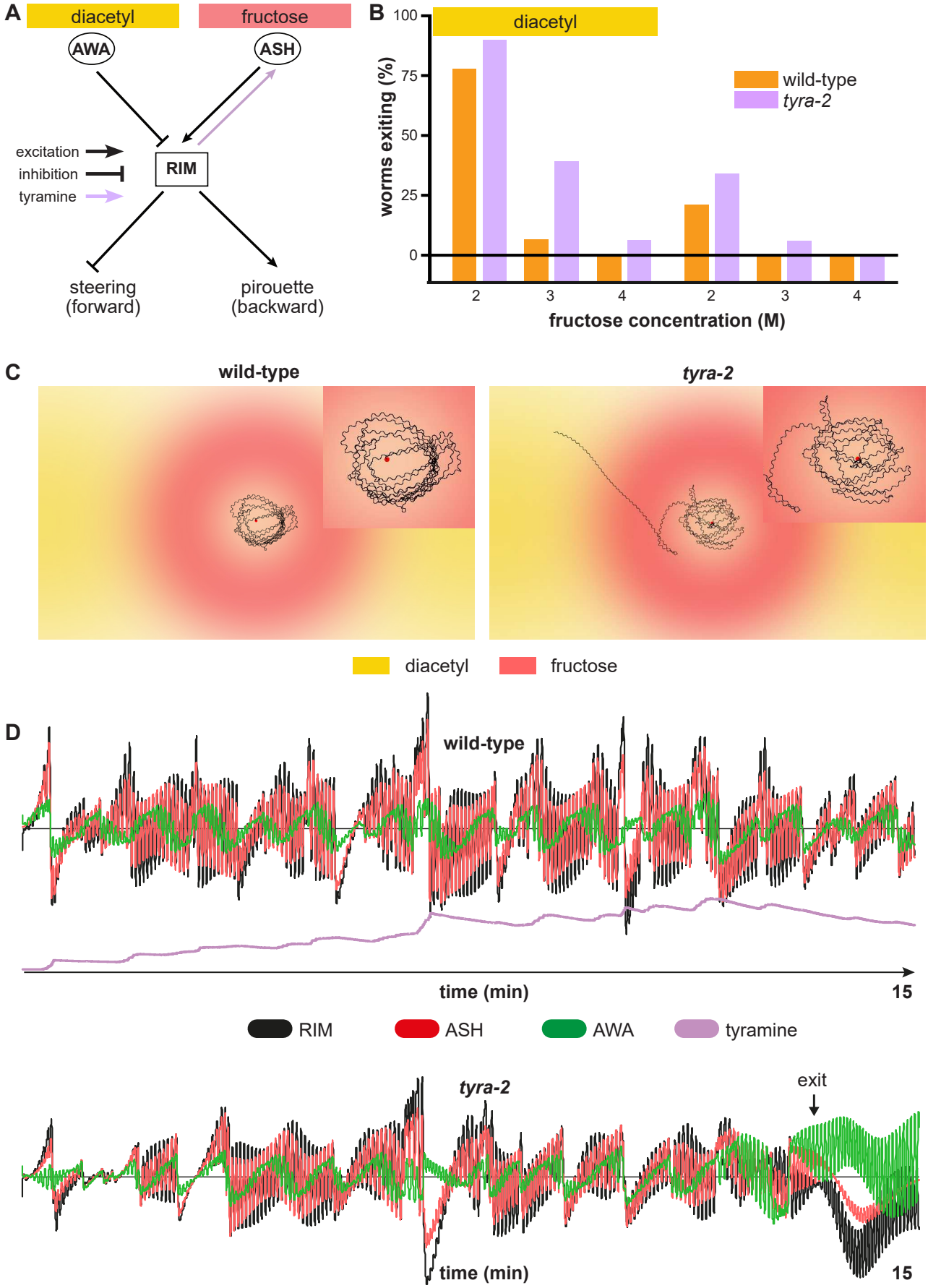
A
diacetyl
fructose
AWA
ASH
excitation
inhibition
tyramine
RIM
steering
(forward)
pirouette
(backward)
B
diacetyl
wild-type
tyra-2
worms exiting (%)
100
75
50
25
0
2
3
4
2
3
4
fructose concentration (M)
C
wild-type
tyra-2
diacetyl
fructose
D
wild-type
time (min)
15
RIM
ASH
AWA
tyramine
tyra-2
exit
time (min)
15

Figure 6

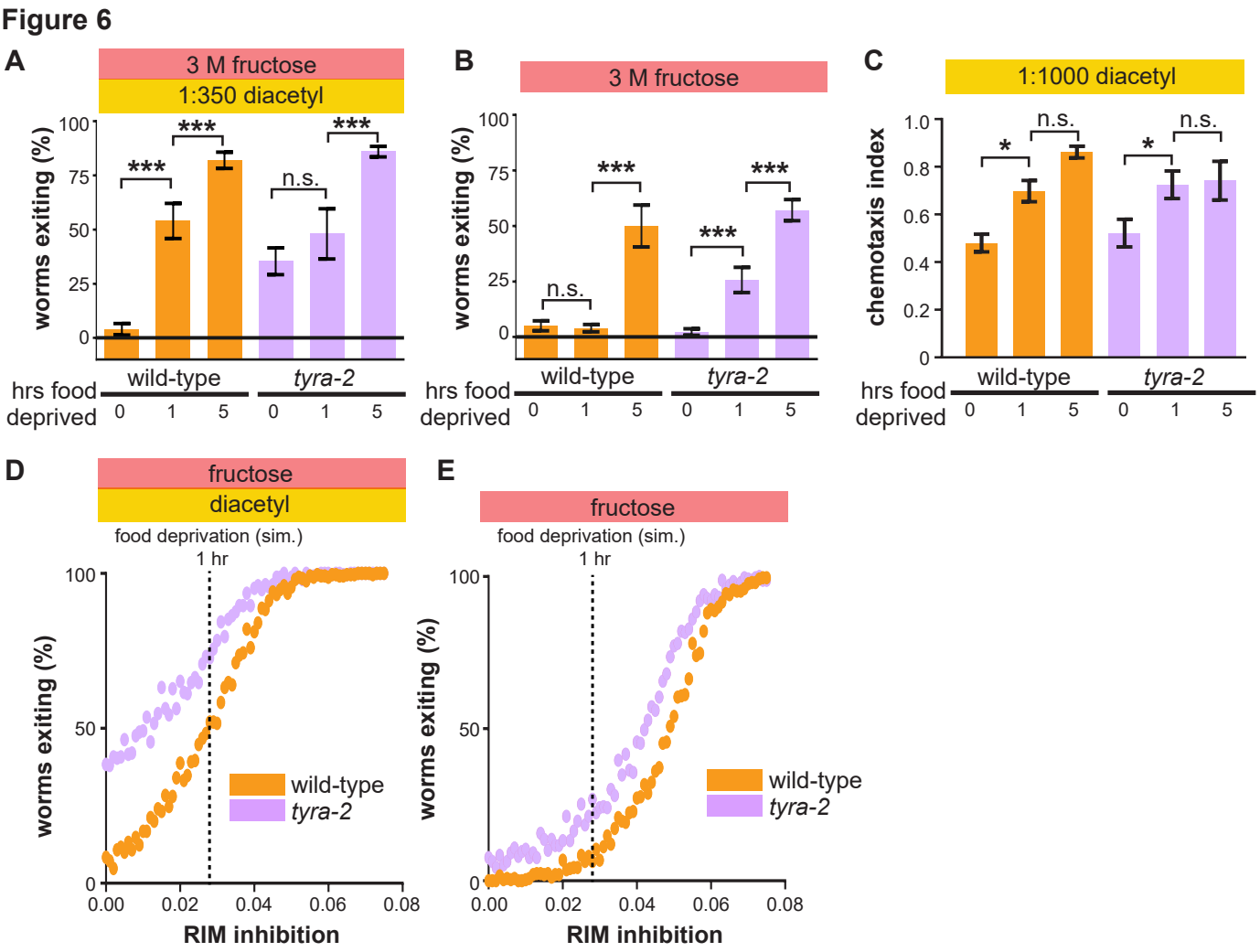
Figure 6
A
3 M fructose
1:350 diacetyl
worms exiting (%)
100
75
50
25
0
***
***
n.s.
***
wild-type
tyra-2
hrs food deprived
0 1 5 0 1 5
B
3 M fructose
worms exiting (%)
n.s.
***
***
***
wild-type
tyra-2
hrs food deprived
0 1 5 0 1 5
C
1:1000 diacetyl
chemotaxis index
1.0
0.8
0.6
0.4
0.2
0
*
n.s.
*
n.s.
wild-type
tyra-2
hrs food deprived
0 1 5 0 1 5
D
fructose
diacetyl
food deprivation (sim.)
1 hr
worms exiting (%)
100
50
0
wild-type
tyra-2
0.00 0.02 0.04 0.06 0.08
RIM inhibition
E
fructose
food deprivation (sim.)
1 hr
worms exiting (%)
100
50
0
wild-type
tyra-2
0.00 0.02 0.04 0.06 0.08
RIM inhibition

Figure 7

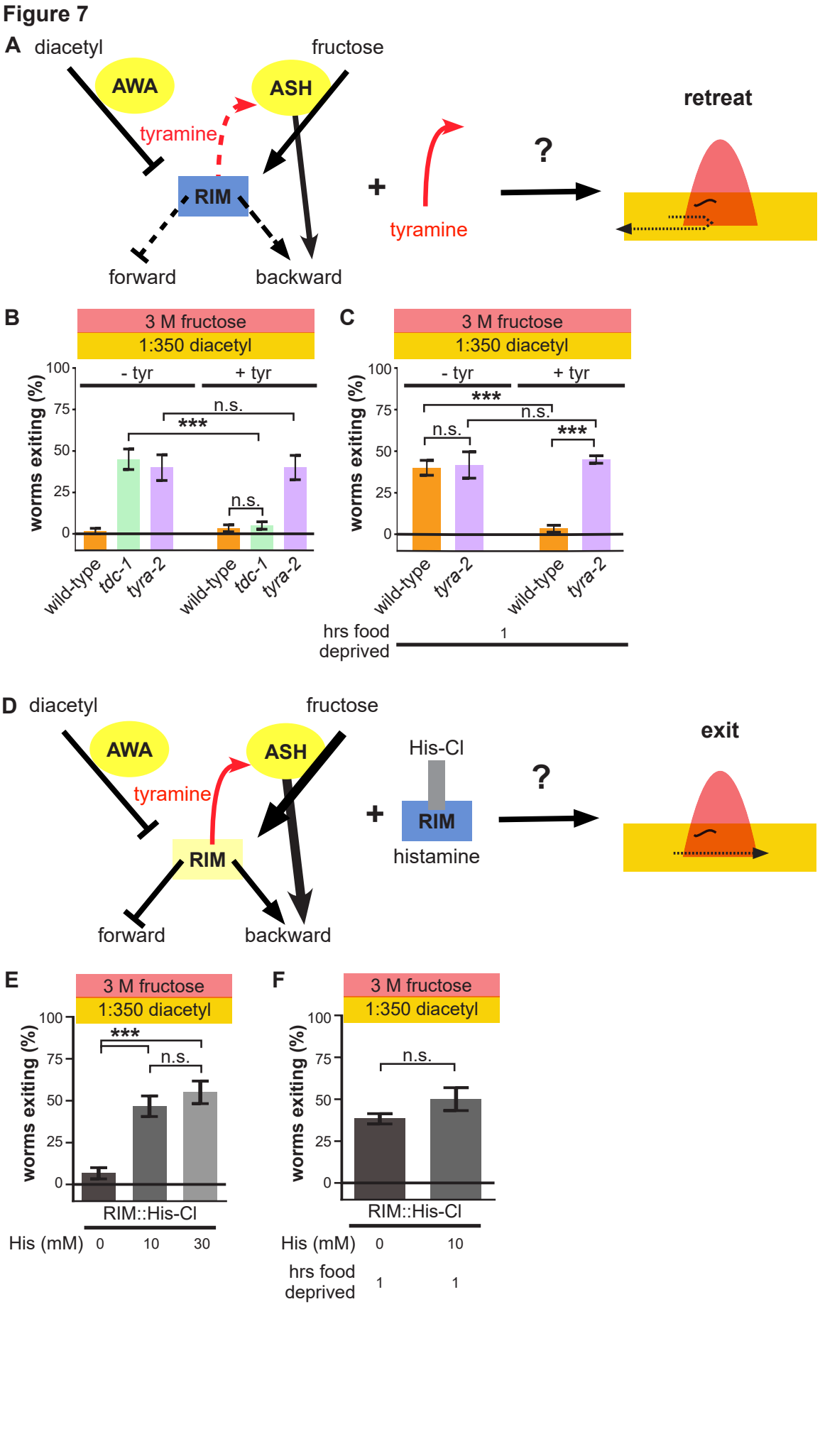
Figure 7
A
diacetyl
fructose
AWA
ASH
tyramine
RIM
forward
backward
+
tyramine
?
retreat
B
3 M fructose
1:350 diacetyl
- tyr
+ tyr
worms exiting (%)
100
75
50
25
0
n.s.
***
n.s.
wild-type
tdc-1
tyra-2
wild-type
tdc-1
tyra-2
C
3 M fructose
1:350 diacetyl
- tyr
+ tyr
worms exiting (%)
***
n.s.
n.s.
***
wild-type
tyra-2
wild-type
tyra-2
hrs food deprived
1
D
diacetyl
fructose
AWA
ASH
tyramine
RIM
forward
backward
+
His-Cl
RIM
histamine
?
exit
E
3 M fructose
1:350 diacetyl
worms exiting (%)
100
75
50
25
0
***
n.s.
RIM::His-Cl
His (mM)
0
10
30
F
3 M fructose
1:350 diacetyl
worms exiting (%)
100
75
50
25
0
n.s.
RIM::His-Cl
His (mM)
0
10
hrs food deprived
1
1

Figure S1

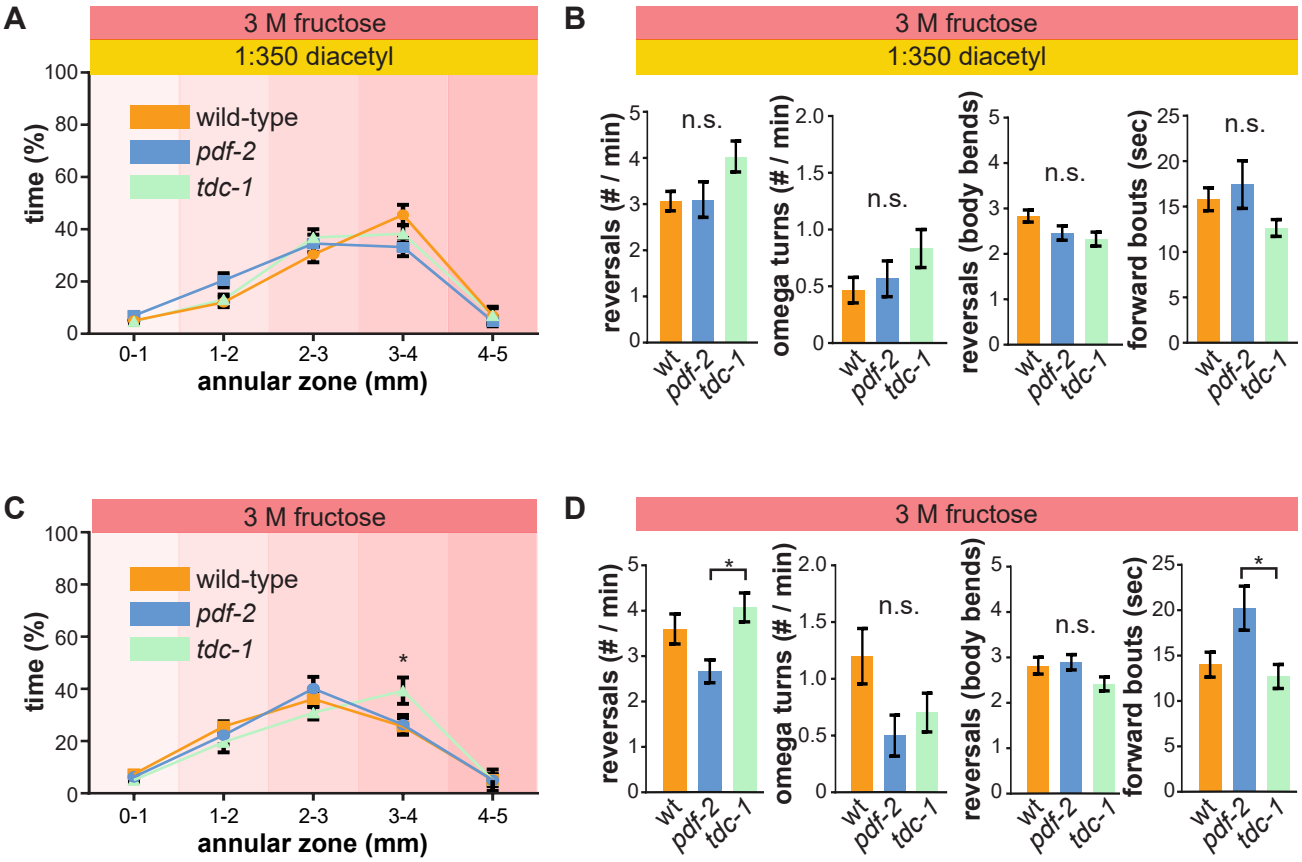
A
3 M fructose
1:350 diacetyl
wild-type
pdf-2
tdc-1
time (%)
annular zone (mm)
0-1
1-2
2-3
3-4
4-5
B
3 M fructose
1:350 diacetyl
reversals (# / min)
omega turns (# / min)
reversals (body bends)
forward bouts (sec)
n.s.
wt
pdf-2
tdc-1
C
3 M fructose
wild-type
pdf-2
tdc-1
time (%)
annular zone (mm)
*
D
3 M fructose
reversals (# / min)
omega turns (# / min)
reversals (body bends)
forward bouts (sec)
*
n.s.

Figure S2

A

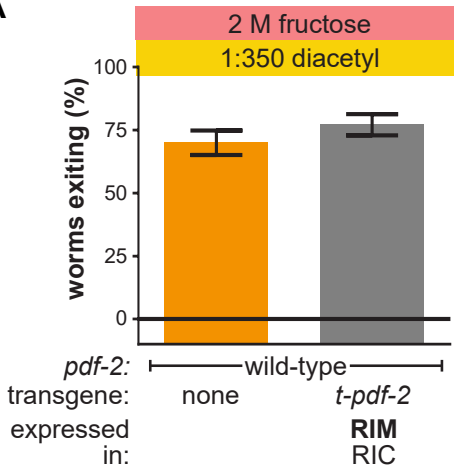
2 M fructose
1:350 diacetyl
worms exiting (%)
100
75
50
25
0
pdf-2:
wild-type
transgene:
none
t-pdf-2
expressed in:
RIM
RIC

Figure S3

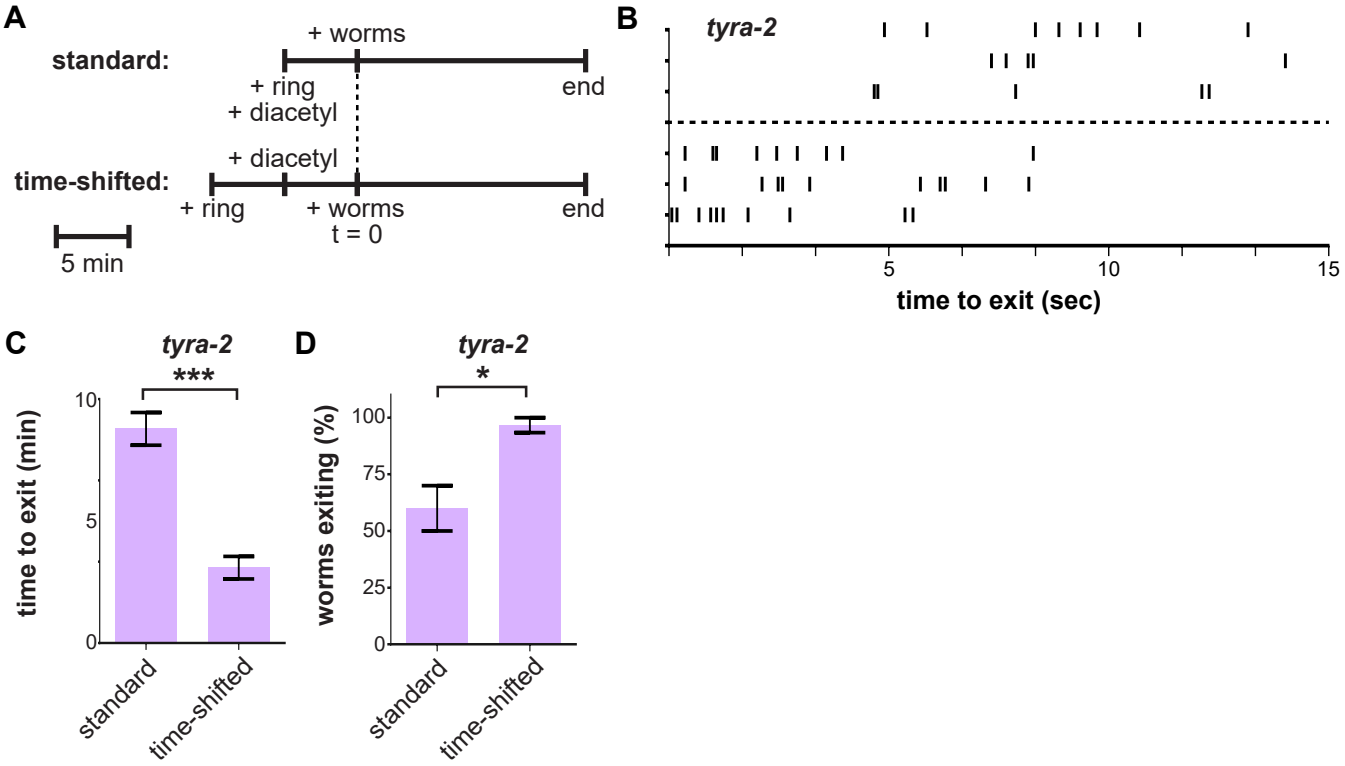
A
standard:
+ worms
+ ring
+ diacetyl
end
time-shifted:
+ diacetyl
+ ring
+ worms
t = 0
end
5 min
B
tyra-2
5
10
15
time to exit (sec)
C
tyra-2
***
time to exit (min)
10
5
0
standard
time-shifted
D
tyra-2
*
worms exiting (%)
100
75
50
25
0
standard
time-shifted

Figure S4

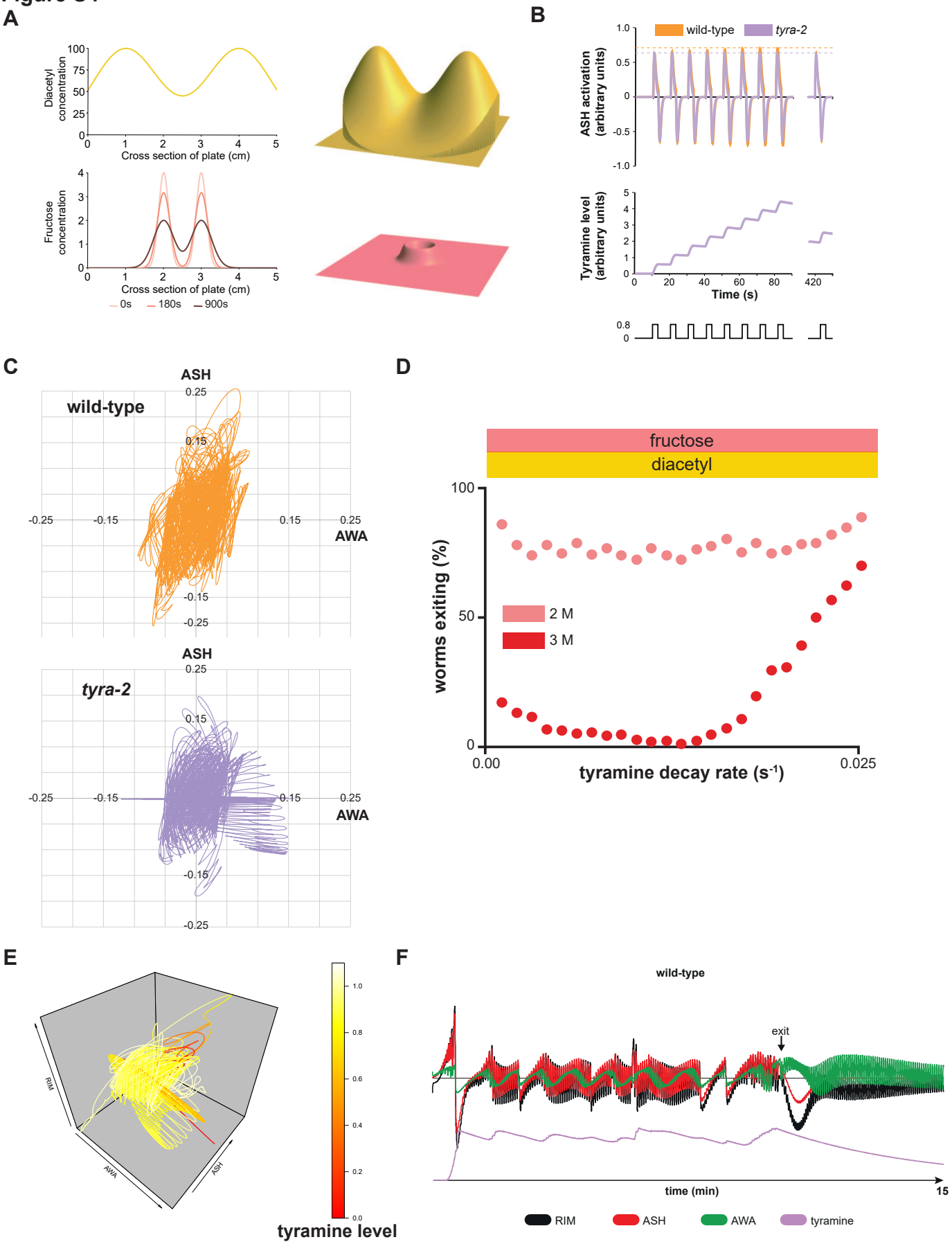
A
Diacetyl concentration
Cross section of plate (cm)
Fructose concentration
Cross section of plate (cm)
0s
180s
900s
B
wild-type
tyra-2
ASH activation (arbitrary units)
Tyramine level (arbitrary units)
Time (s)
C
ASH
wild-type
AWA
ASH
tyra-2
AWA
D
fructose
diacetyl
worms exiting (%)
2 M
3 M
tyramine decay rate (s-1)
E
RIM
AWA
ASH
tyramine level
F
wild-type
exit
time (min)
RIM
ASH
AWA
tyramine

Figure S5

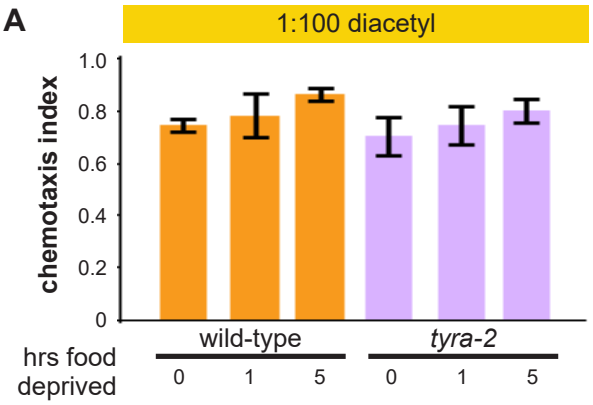
A
1:100 diacetyl
chemotaxis index
1.0
0.8
0.6
0.4
0.2
0
wild-type
tyra-2
hrs food deprived
0
1
5
0
1
5

Figure S6

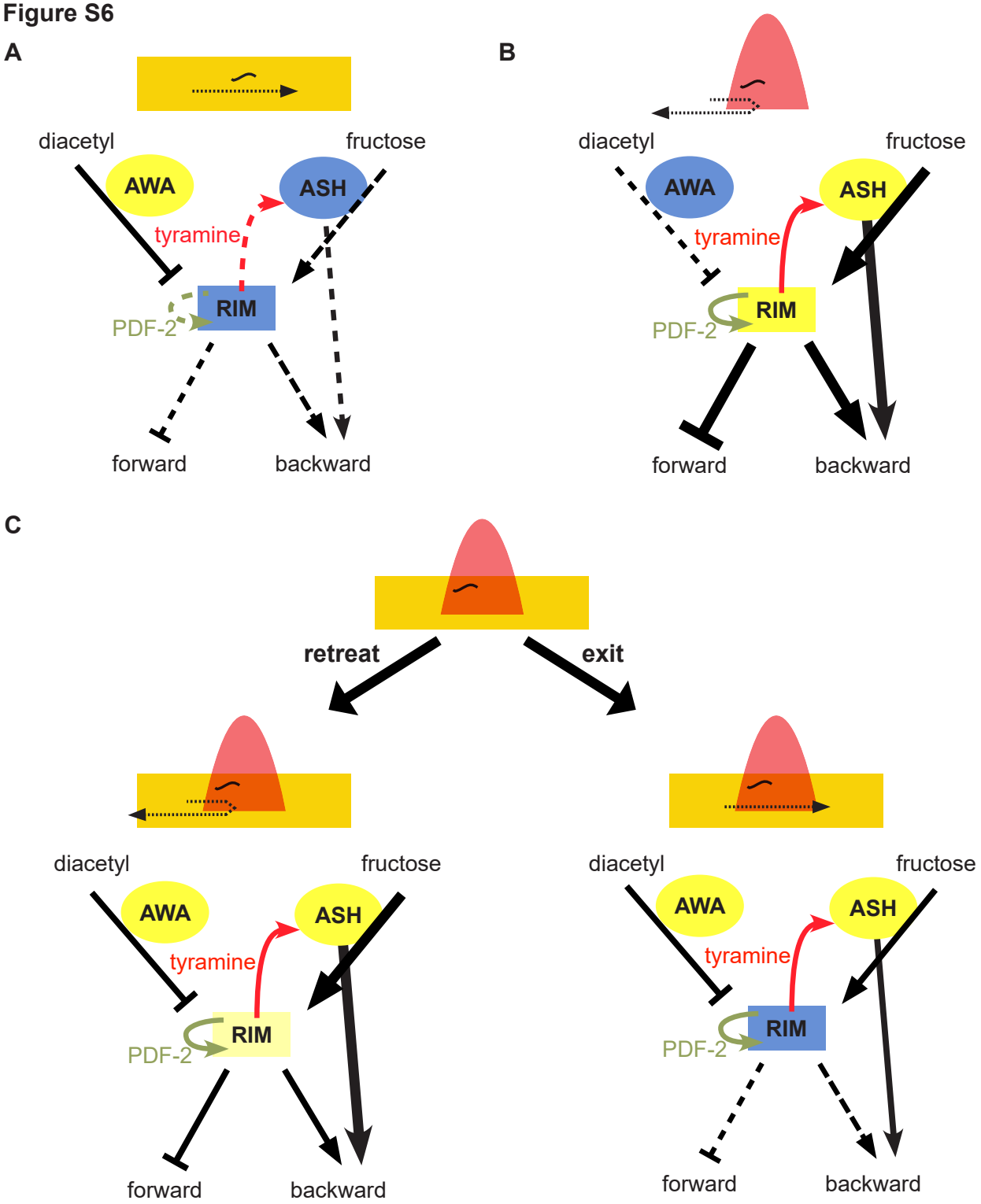
A
diacetyl
fructose
AWA
ASH
tyramine
RIM
PDF-2
forward
backward
B
diacetyl
fructose
AWA
ASH
tyramine
RIM
PDF-2
forward
backward
C
retreat
exit
diacetyl
fructose
AWA
ASH
tyramine
RIM
PDF-2
forward
backward
diacetyl
fructose
AWA
ASH
tyramine
RIM
PDF-2
forward
backward

Figure S1, related to Figures 2,3. Kinematic analysis of *pdf-2* and *tdc-1* null mutants

(A) Wild-type, *pdf-2*, and *tdc-1* null-mutant worms spend indistinguishable fractions of time in each of the radial zones of the osmotic ring in the presence of food odor. This excludes the potential confound that wild-type and mutant worms spend different amounts of time near the barrier, and thus have an altered opportunity to interact with it. (n=7-10 worms for each genotype, F = 1.273, p = 0.265)

(B) General defects in locomotion are not involved in aberrant multisensory decision making by *pdf-2* and *tdc-1* null-mutant worms. Kinematic parameters are indistinguishable between wild-type, *pdf-2* and *tdc-1* null-mutant worms as they navigate within the ring in the multisensory context.

(C) Wild-type and *pdf-2*, but not *tdc-1* null-mutant worms, spend indistinguishable fractions of time in each of the radial zones of the fructose ring in the absence of food odor (N=7-10 worms for each genotype, F = 2.510, p = 0.015). *tdc-1* null-mutant worms spend increased time in the 3-4 mm radial zone (*, p vs wild-type = 0.009).

(D) *pdf-2* and *tdc-1* null-mutant worm locomotor kinematics differ from one another as they navigate within the ring in the absence of food odor.

Figure S2, related to Figure 3. PDF-2-PDFR-1 autocrine loop is maximally active

(A) Expression of t-PDF-2 in RIM and RIC in a wild-type background did not suppress exiting of a 2 M fructose ring in the presence of diacetyl.

Figure S3, related to Figure 4. Diffusion of osmotic ring determines time to exit

(A) Schematic depicting protocols for determining effect of diffusion of osmotic ring on time to exit. Worms were either confronted with standard or time-shifted osmotic rings. Time-shifted rings are allowed five more minutes to diffuse than standard rings.

(B) Ethogram of time-to-exit reveals that *tyra-2* null-mutant worms exit time-shifted rings earlier than standard rings.

(C) Average time-to-exit of *tyra-2* null-mutant worms. Worms exit time-shifted rings approximately five minutes before standard rings.

(D) More worms exit time-shifted rings than standard rings in the 15 minute trial.

Figure S4, related to Figure 5. Time constants of accumulation and decay of tyramine signals determine multisensory decision balance

(A) Profiles of diacetyl and fructose concentration in simulated decision arena. While the bilobed diacetyl gradient is modeled as invariant over the time course of the decision, the simulated fructose gradient becomes shallower over time.

(B) Model ASH responses to repetitive fructose stimulation. In wild-type worms, the ASH response increases with every consecutive stimulus presentation due to increasing tyramine levels. This effect is not observed in *tyra-2* null-mutants. That tyramine potentiates ASH osmosensitivity by acting on TYRA-2 is somewhat surprising given that TYRA-2 has been characterized as a $G_{i/o}$-coupled receptor (Rex et al., 2005). However, invertebrate tyramine receptors have demonstrated the capacity to signal through $G_{i/o}$ while still increasing intracellular calcium (Rex et al., 2005; Rex and Komuniecki, 2002; Rex et al., 2004; Wragg et al., 2007).

(C) 2D phase space profile of ASH (y-axis) and AWA (x-axis) neuronal activity in a virtual wild-type worm (top) that remains inside the ring for the duration of the assay and a *tyra-2* null-mutant worm (bottom) that exits the ring. These phase space profiles demonstrate how the magnitude of ASH oscillatory activity is greater in wild-type

worms than in *tyra-2* null-mutant worms; in contrast, in *tyra-2* null-mutant worms, the AWA signals are larger, before dominating as the worm exits.

(D) Slow tyramine signals (decay constants of $0.001s^{-1}$ to $0.025s^{-1}$) in the model are necessary for wild-type worms to remain confined in the 3 M fructose ring, as observed experimentally. As tyramine decay becomes faster, wild-type worms begin exiting in substantial numbers. *n*=250 simulated worms per genotype and condition.

(E) 3D phase space profile of neuronal activity and tyramine level in a virtual wild-type worm that exits a 3 M fructose ring in the presence of diacetyl, with RIM inhibited to ~0.03 to simulate one-hour of food deprivation. This analysis (shown dynamically in **Supplemental Movie 1**) demonstrates several distinct phases in neuronal activity over the course of the decision. Progression through the phases depends on accumulation of tyramine signals that reinforce ASH activity upon repeated encounters with the ring. Initial oscillations are primarily in the ASH-RIM plane (red) as the animal nears and retreats from the fructose ring, leading to a slow accumulation of tyramine (white). The gradual diffusion of the fructose ring eventually results in the decay of tyramine levels and activity in RIM and ASH responses (yellow, then orange). Phase space oscillations get smaller, and tilt toward the AWA-RIM plane, indicating a desensitization of ASH and potentiation of AWA as the worm continues to approach the ring. Exiting of the ring follows a dip in tyramine levels after nine minutes (yellow-orange). AWA activity begins to dominate, despite the subsequent rapid increase in tyramine and strong RIM-ASH oscillations as the animal exits the ring (white). As the worm crosses the peak of the fructose ring, it encounters the steepest diacetyl gradient, as indicated by the significant increase in AWA activity. Once outside the ring, AWA then decreases again as the worm navigates towards the diacetyl spot. Once the animal reaches the diacetyl spot, both ASH and AWA activity levels decay and ASH activity is nearly abolished (red).

(F) Neural activity and tyramine signal profiles of AWA, ASH, and RIM in a virtual wild-type worm that exits a 3 M fructose ring in the presence of diacetyl, with RIM inhibited to ~0.03 to simulate one-hour of food deprivation, corresponding to phase space profile depicted in **(D)**.

Figure S5, related to Figure 6. Chemotaxis to 1:100 diacetyl after food deprivation

(A) Chemotaxis to 1:100 diacetyl is unaffected by food deprivation.

Figure S6, related to Figure 7. Model for sensorimotor network control of multisensory threat-reward decision making

(A) In the unisensory attraction-only context, AWA inhibits RIM and RIM neither inhibits forward command nor excites backward command interneurons. Thus, the worm proceeds forward up the diacetyl odor gradient. Yellow represents strong activity, while blue represents weak activity. Thickness of solid lines represents strength of signals, and dashed lines represent inactive signals. Other synaptic routes by which AWA and ASH indirectly communicate with forward and backward command locomotor interneurons are not shown.

(B) In the unisensory aversion-only context, ASH activates RIM, triggering tyraminergic RIM-ASH positive feedback and further potentiating ASH osmosensitivity. This combined strong ASH and RIM activation strongly inhibits forward command and strongly excites backward command interneurons. Thus, the worm reverses and retreats from the osmotic barrier. However, because of the absence of AWA-mediated inhibition of RIM in the unisensory aversion-only context, RIM-ASH feedback is not required for retreat from the osmotic barrier.

(C) In the multisensory context where RIM is both inhibited by AWA and activated by ASH, the worm makes a probabilistic choice between retreat and exit based on the instantaneous stochastic state of the network as it interacts with the osmotic barrier. An increase in RIM activity state leads to reversal behaviors that promote retreat from threats; however, these reversal behaviors are probabilistic because instantaneous activity state of RIM itself is stochastic (Gordus et al., 2015). When instantaneous network activity is strong, combined RIM and ASH activity inhibits forward command and activates backward command interneurons to trigger a reversal and retreat from the osmotic barrier. When instantaneous network activity is weak, combined RIM and ASH activity is insufficient to inhibit forward command and excite backward command interneurons, and the worm proceeds forward through the barrier to exit the ring. Autocrine PDF-2 signaling to RIM increases the gain of the RIM-ASH positive feedback

loop, and is suppressed by food deprivation to increase threat tolerance. Longer time-scale tyraminergic feedback increases the likelihood that instantaneous RIM and ASH network activity is strong. Disruptions that break the positive feedback loop increase threat tolerance in the multisensory context by allowing AWA-mediated inhibition of RIM to dominate and prevent reversals.

Supplemental Movie, related to Figures 5,6 (Online-only)

(A) Phase space profile of neuronal activity and tyramine levels in a virtual wild-type worm that exits a 3 M fructose ring in the presence of diacetyl, with RIM inhibited to ~0.03 to simulate one-hour of food deprivation. Left: 10 second sliding window of AWA, ASH, and RIM activity levels, plotted in phase space. Color represents tyramine level. Top right: Corresponding time traces of AWA and ASH. Bottom right: simulated worm trajectory over the course of the decision. Note that the concentration gradient of fructose changes over time.

Supplemental Experimental Procedures

Strains

C. elegans strains were maintained on Nematode Growth Medium (NGM) agar plates with *E. coli* OP50 as a food source. All strains were derived from the Bristol N2 wild-type strain. Each strain was backcrossed to the wild-type N2 at least 3 times. At least three independent lines for all transgenic strains were generated and tested, and presented results are aggregates of the independent lines. Strains used for each figure are detailed below:

Figure 1: N2, *odr-10 (ky225)*

Figure 2: N2, CX14484 *pdf-2(tm4393)*, MNN1 *pdf-2(tm4393)*; *lin-15(n765ts)*; *mnnEx1 [pdf-2p::pdf-2; lin-15^{+}]*

Figure 3: N2, CX14484 *pdf-2(tm4393)*, MNN2 *pdf-2(tm4393)*; *lin-15(n765ts)*; *mnnEx2 [tdc-1p::pdf-2; lin-15^{+}]*, MNN3 *pdf-2(tm4393)*; *lin-15(n765ts)*; *mnnEx3 [tdc-1p::t-pdf-2; lin-15^{+}]*, MNN4 *pdf-2(tm4393)*; *lin-15(n765ts)*; *mnnEx4 [nmr-2p::t-pdf-2; lin-15^{+}]*, MNN5 *pdf-2(tm4393)*; *lin-15(n765ts)*; *mnnEx5 [tbh-1p::t-pdf-2; lin-15^{+}]*, MNN6 *pdf-2(tm4393)*; *lin-15 (n765ts)*; *mnnEx6 [tdc-1p::t-scr; lin-15^{+}]*, MT13113 *tdc-1(n3419)*, MT9455 *tbh-1(n3247)*, MNN10 *pdf-2 (tm4393); tdc-1 (n3419)*

Figure 4: N2, MT13113 *tdc-1(n3419)*, QW245 *lgc-55(tm2913)*, VC125 *tyra-3(ok325)*, OH313 *ser-2 (pk1357)*, QW42 *tyra-2(tm1815)*, MNN7 *tyra-2(tm1815)*; *mnnEx7 [sra-6p::tyra-2; myo-3p::gfp]*, MNN8 *tyra-2(tm1815)*; *mnnEx8 [gpa-13p::tyra-2; myo-3p::gfp]*; MNN9 *tyra-2(tm1815)*; *mnnEx9 [mec-17p::tyra-2; myo-3p::gfp]*, XP631 *lite-1(ce314); kyEx2865 [sra-6p::GCaMP3, unc-122p::gfp]*; XP649 *lite-1(ce314); tyra-2(tm1846)*; *kyEx2865 [sra-6p::GCaMP3, unc-122p::GFP]*, MNN11 *pdf-2 (tm4393); tyra-2(tm1815)*

Figure 6: N2, QW42 *tyra-2(tm1815)*

Figure 7: N2, MT13113 *tdc-1(n3419)*, QW42 *tyra-2(tm1815)*, CX16632 *kyIs693 [pNP502(tdc-1::HisCl1::sl2::mcherry)]*

Supplemental Figure 1: N2, CX14484 *pdf-2(tm4393)*, MT13113 *tdc-1(n3419)*

Supplemental Figure 2: N2, MNN12 N2; *mnnEx9 [tdc-1p::t-pdf-2; myo-3p::gfp]*

Supplemental Figure 3: N2, QW42 *tyra-2(tm1815)*

Supplemental Figure 5: N2, QW42 *tyra-2(tm1815)*

Tethered peptides were designed as described previously (Choi et al., 2012; Choi et al., 2009; Choi and Nitabach, 2013; Fortin et al., 2009). Briefly, tethered peptides are chimeric fusion proteins with an N-terminal secretory signal sequence, followed by the sequence of the peptide of interest, a linker, and a C-terminal glycolipid anchor targeting signal. Tethered peptide transgenes were synthesized by Entelechon. Transgenes were synthesized with optimal *C. elegans* codon usage and optimal upstream Kozak sequences.

Amino acid sequences for construction of tethered peptides are as follows (peptide is **bold**, * indicates stop codon):

t-PDF-2:

MSALLILALVGAAVA**NNAEVVNHILKNFGALDRLGDV**GNEQKLISEEDLGNGAGFATPVTLALVPALLA TFWSLL*

t-SCR:

MSALLILALVGAAVA**VIALDNKRNLNFENGAVGVHLD**GNEQKLISEEDLGNGAGFATPVTLALVPALLA TFWSLL*

Transgenic strains were constructed by injection of plasmid DNA into the germline according to standard practice. Plasmid DNA was engineered using Multisite Gateway Cloning technology (Invitrogen, http://www.lifetechnologies.com/us/en/home.html). *pdf-2*, *t-pdf-2*, *t-scr*, and *tyra-2* protein coding sequences were cloned into pDONR-221 vectors. These were linked with cell-specific promoters *pdf-2*, *tdc-1*, *nmr-2*, *tbh-1*, *sra-6*, *gpa-13*, and *mec-17*. Promoters were generated by amplifying genomic DNA using Promoterome sequences (http://worfdb.dfci.harvard.edu/promoteromedb/) or published primer sequences and cloning them into pDONR-P4-P1R vectors. These were then integrated into final vectors, and injected at concentrations of 20-50 ng/µL. A *lin-15* rescue construct pL15EK or *myo-3::GFP* construct was co-injected to mark transformation.

Behavioral assays

For unisensory and multisensory assays, the fructose ring was constructed essentially as described (Culotti and Russell, 1978). Briefly, 10µL of fructose solution is applied in a 1cm diameter ring centered on a standard NGM plate. For multisensory assays, 1µL diluted diacetyl (1:350 in water) was applied to each side of the plate, at least 1cm from the ring border. Four minutes after construction of the ring, ten (unless otherwise indicated) 18-24 hours post-L4 stage adult worms were removed from a food plate, placed on a plate without food to remove attached bacteria, and then quickly transferred inside the ring. Fifteen minutes later, the number of worms outside the ring were counted. For the food deprivation assays, worms were transferred to a plate without food to remove attached bacteria, then quickly transferred to another plate without food for the indicated time interval. 10 mM or 30 mM histamine and 30 mM tyramine plates were prepared exactly as described previously (Jin et al., 2016; Pokala et al., 2014).

Chemotaxis assays were performed essentially as described, with minor changes from (Sengupta et al., 1996), as described below. First, a standard sized (5 cm) NGM plate was used. Second, similar to the multisensory assay, ten staged adult worms were placed at a location equidistant to the two spots, control and test, applied to either side of the plate. To remain consistent with the multisensory assay, chemotaxis was measured after 15 minutes. One-way ANOVA with Tukey-Kramer *post-hoc* test was used for statistical comparison with wild-type worms.

For kinematic analysis, assays prepared as detailed above were recorded using a Point Grey Grasshopper camera (GRAS-50S5C-C) filming at 7.5 fps. Dishes were illuminated with a red LED ring obtained from Moritex Schott (Model RLA-75X46-00R). These videos were then analyzed using commercially available WormLab software from MBF Bioscience (http://www.mbfbioscience.com/wormlab). Software provided *x-y* position information. A picture of the ring, taken immediately after the assay, was used to determine the center of the ring. Distance from the center of the ring was then calculated and sorted into annular zones. Two-way ANOVA with a *post-hoc* Tukey-Kramer test was used to determine statistically significant differences from wild-type. Other locomotor parameters were manually scored as previously described (Alkema et al., 2005; Donnelly et al., 2013; Gray et al., 2005; Pirri et al., 2009).

Imaging

Calcium imaging of ASH neurons was performed on young adult *lite-1 (ce314)* worms immobilized in an olfactory chamber as described previously (Chronis et al., 2007). Imaged worms expressed the genetically-encoded calcium sensor GCaMP3 from the *sra-6* promoter (Tian et al., 2009). Prior to loading into the olfactory chamber worms were bathed in neuronal buffer (10mM HEPES pH 7.1, 40mM NaCl, 1mM $MgSO_4$, 1mM tetramisole) for 10 min either in the presence or absence of 50mM tyramine. Once in the chamber worms were exposed to a laminar flow of neuronal buffer (with or without tyramine) for at least 10 sec before switching flow in the chamber to direct the test stimulus across the animal's nose (diluted in neuronal buffer containing 1mg/ml bromophenol blue). Bromophenol blue was added to monitor test stimulus flow and had no effect on ASH activity. Worms were exposed to the test stimulus for 20 sec. All imaging experiments were performed using a Nikon FN1 microscope equipped with a 40x water immersion objective. Images were captured at ~10Hz using a Photometrics CoolSnap EZ camera with a single frame exposure time of 100ms. Averaged fluorescence was calculated for a region of interest (ROI) surrounding the ASH soma and was background corrected using NIS Elements AR software. The percent change in fluorescence for each frame was calculated relative to the corrected fluorescence of the ROI just prior to stimulus onset.

Computational model

Model animals possess a simplified nervous system comprising sensory neurons AWA and ASH, interneuron RIM, and two reciprocally inhibited motor neurons denoted DMN and VMN, which activate dorsal and ventral body bends, respectively. Neurons are modeled as "leaky integrators," such that each neuron integrates its input over time, while subject to continuous decay ("leak") of activity. AWA and ASH sensory neurons respond with transient activation to changes in diacetyl or fructose stimuli, respectively. These transients were modeled with a fast depolarizing signal, which drives a delayed rectifying counter-signal. This sensory response was adapted from chemotaxis models in unicellular eukaryotes, in which the delayed signal modeled intracellular diffusion (Cohen and Sanders, 2014; Levine and Rappel, 2013). Neuronal time scales were set in accordance with calcium imaging data (Kato et al., 2014), and were fast enough to mediate steering responses on time scales of an undulation. Activation of model sensory neurons AWA and ASH instantaneously provides differentially weighted inhibitory and excitatory inputs onto RIM, respectively. RIM integrates these sensory inputs and inhibits motorneurons DMN and VMN to bias dorsal versus ventral bends, thereby inducing gradual steering of the worm. Additionally, RIM activity positively increases the likelihood of pirouettes, which are modeled as instantaneous step changes in angular heading. In the absence of sensory input, the model worm's dorsoventral undulatory locomotion is driven by stable oscillations of a simplified central pattern generating circuit consisting of DMN and VMN. The animals move forward along an undulating path at a fixed speed of 0.11mm/s, interrupted by occasional stochastic turning events (average pirouette rate of 2.1 turns/min). Sensory input allows both steering (klinotaxis), by biasing the oscillator, and a "tumble-and-run" strategy (klinokinesis), by varying the pirouette probability. Importantly, in addition to the above previously established feedforward sensorimotor pathways, the simulation includes RIM-ASH tyraminergic positive feedback. Tyraminergic potentiation of ASH in the model is only engaged above a threshold level of RIM activation (see **Equation M3**). This non-linear relationship ensures that the RIM-ASH positive feedback loop is activated only in response to sufficiently aversive stimuli, a feature of the model that is necessary to successfully reproduce experimental exiting rates. The TYRA-2 receptor in ASH promotes ASH sensitivity to osmotic stimuli in the presence of tyramine, but with no direct effect on the ASH membrane potential. *tyra-2* null-mutant worms are modeled as lacking this tyraminergic feedback to ASH. Food deprivation was modeled as direct inhibition of RIM activity.

Model parameters were manually calibrated until exiting rates of simulated wild-type and *tyra-2* null-mutant worms matched experimental exiting rates in multisensory and unisensory contexts for 2 M, 3 M, and 4 M fructose (compare **Figure 2B** with **Figure 5B**). Specifically, model parameters subject to calibration comprise: the strengths of the AWA-RIM and ASH-RIM synapses, the tyramine accumulation rate, the tyramine decay rate, and the threshold activity value above which tyramine is secreted from RIM. Of these, the first two were constrained by the experimental exiting rates of *tyra-2* null-mutant worms in the multisensory and unisensory contexts; the latter three were then calibrated to match the experimental exiting rates of wild-type worms in those same contexts.

The virtual decision arena comprises a continuously diffusing fructose gradient ring and time-invariant diacetyl gradients originating from two spots outside the ring (**Figure S4A**). Modeling the fructose gradient as dynamically changing was essential, as continued diffusion of the fructose ring influences the time and probability of exit in our experiments (**Figure S3**), and static fructose gradients failed to reproduce experimental exiting rates in the model. Each simulation begins with a single worm in the center of the virtual arena with a randomly selected initial heading, and the simulation is allowed to proceed for fifteen virtual minutes.

See accompanying **Supplemental Experimental Procedures** section for more details.

Supplemental References

Cohen, N., and Sanders, T. (2014). Nematode locomotion: dissecting the neuronal-environmental loop. Curr Opin Neurobiol *25*, 99-106.

Kato, S., Xu, Y., Cho, C.E., Abbott, L.F., and Bargmann, C.I. (2014). Temporal responses of C. elegans chemosensory neurons are preserved in behavioral dynamics. Neuron *81*, 616-628.

Levine, H., and Rappel, W.J. (2013). The physics of eukaryotic chemotaxis. Phys Today *66*.

Supplemental Experimental Procedures

Computational model

A computational simulation framework was developed to study *in silico* the behavior of single model worms confronted with the decision making assay. Our model of the animal assumes that during locomotion, the body follows the head, allowing us to focus on sensory-motor control of a point worm. Thus, at each point in time, animals are represented by their point coordinates $\vec{r}(t) = (x(t), y(t))$ and heading $\theta(t)$. Animals move at fixed speed and sense their environment using a simplified nervous system which dynamically controls their direction of locomotion.

Our computational model extends a previously developed *C. elegans* sensorimotor model that was extensively tested against a number of assays (Sanders T., PhD thesis 2016). To study sensory integration, our new model circuit contained two sensory neurons (AWA and ASH) and one interneuron (RIM) as well as a simplified motor system (Fig. M1). The motor output consists of undulations that are modulated by the sensory system to generate steering, and instant turning events representing pirouettes. All neuronal equations and parameters, including the sensory responses, interneuron and motor neuron dynamics were taken without modification from our previous model, in which they were constrained by calcium imaging data (Thiele et al., 2009; Larsch et al., 2013) and published behavioral data (Iino and Yoshida, 2009; Jansen et al., 2002; Hukema et al., 2006, 2008).

To extend the model to cope with sensory integration, we began by modeling the assay environment and specifically the fructose and diacetyl concentration profiles over time (Fig. M3). The addition of RIM to our model circuit required synaptic connections from ASH and from AWA onto RIM. The two synaptic weights were set by matching behavioral data from *tyra-2* animals (Fig. 5). Next, RIM's tyramine accumulation threshold and the tyramine accumulation and decay rates were set, based on behavioral results from wild type animals (Fig. 5). Thus, only five of the model parameters were free. One additional variable (the RIM rest potential) was needed to capture food deprivation results; the corresponding results are presented as a parameter sweep. This incremental modeling approach ensures the model is maximally constrained and is aimed at enhancing its predictive potential.

1.1 Model neurons

As the AWA, ASH and RIM Left/Right neuronal pairs are all coupled by gap junctions (White et al., 1986) and ASH Left and Right neurons are known to respond identically (Thiele et al., 2009), all three neuron pairs have been collapsed into single model neurons. We model all neurons as leaky integrators (with arbitrary units)

$$\tau_m \frac{dV_i}{dt} = -V_i + V_{0,i} + \sigma\left(I\right), \tag{M1}$$

where V_i is a voltage like variable for neuron i, also referred to here as neuronal activity; τ_m is a neuronal time constant; finally, $V_{0,i}$ represents the resting potential (set at 0). $\sigma(I)$ is a modified sigmoid function over the input

$$\sigma\left(I\right) = \tanh\left(bI\right), \tag{M2}$$

where b is a gain parameter. Thus a neuron's activation ranges from -1 to 1 and converges to $V_{0,i} + \sigma(I)$ with a timescale of τ_m. This formulation is borrowed from rate neuron models

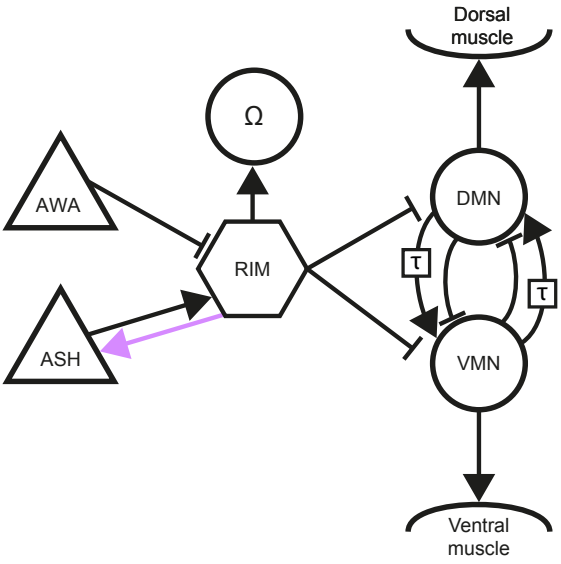

Figure M1: *The model sensorimotor system consists of two sensory neurons, AWA and ASH (triangles), a single interneuron, RIM (hexagon), and a motor circuit (circles). RIM integrates over inputs from the sensory neurons and projects to all three units of the motor circuit. The extrasynaptic neuropeptide tyramine mediates the feedback signal from RIM to ASH. A half-center oscillator (DMN, VMN) acts as a central pattern generator for ongoing undulations that is subject to a steering bias from the sensory inputs. The delay τ is modeled as an implicit neuron. The muscles are included in the diagram for ease of visualization only. An abstract turn component Ω drives pirouettes.*

and naturally leads to thresholding and saturation of activation, as observed in *C. elegans* sensory neurons (Suzuki et al., 2008; Thiele et al., 2009; Larsch et al., 2013).

The input term I sums over all synaptic and sensory contributions $I = I_{\text{syn}}(t) + I_{\text{sens}}(t)$, where $I_{\text{syn}} = \sum_j w_{ij} V_j$ is a weighted sum over all presynaptic neuron activations. The sensory contributions I_{sens} are given in Equations (M5)–(M7). Note that since synapses are not rectified, hyperpolarizing a neuron will effectively reverse the sign of its synaptic outputs (with hyperpolarizing and depolarizing postsynaptic transmission across excitatory and inhibitory synapses respectively). Food deprivation is modeled as sustained inhibition of RIM, by suppressing the RIM resting potential, $V_{0,\text{RIM}}$. The tyramine signal, denoted here $T(t)$, is modeled according to

$$\frac{dT}{dt} = \alpha_{\text{tyr}} H(V - V_{\text{tyr}}) - \beta_{\text{tyr}} T \,, \tag{M3}$$

where the function $H(x) = x$ for $x > 0$ and 0 otherwise. In other words, the tyramine level $T \geq 0$ at all times and increases only when RIM activity is above an activity threshold V_{tyr}.

Neuron parameters	Value	Description
τ_m	0.5 s	Neuronal time constant
$V_{0,i}$	0	Resting potential
b	2	Activation gain factor (used in sigmoid function)
α_{tyr}	$0.4\,\text{s}^{-1}$	Tyramine integration rate
β_{tyr}	$0.004\,\text{s}^{-1}$	Tyramine decay rate
V_{tyr}	0.05	Tyramine accumulation threshold
Synaptic weights	**Value**	**Description**
$w_{\text{AWA,RIM}}$	-0.4	AWA onto RIM
$w_{\text{ASH,RIM}}$	0.75	ASH onto RIM
$w_{\text{RIM,XMN}}$	-0.5	RIM onto DMN and VMN
$w_{\text{RIM},\Omega}$	1	RIM onto Ω
$w^{+}_{\text{D,V}}$	0.88	DMN to VMN excitation (to, from hidden neuron)
$w^{+}_{\text{V,D}}$	0.88	VMN to DMN excitation (to, from hidden neuron)
$w^{-}_{\text{D,V}}$	-1.4	DMN to VMN inhibition
$w^{-}_{\text{V,D}}$	-1.4	VMN to DMN inhibition

1.1.1 RIM inhibition

As mentioned above, food deprivation was mimicked in our model using a single pathway: sustained RIM inhibition, implemented as a modulated RIM resting potential $V_{0,\text{RIM}} \leq 0$. To parametrize the food deprivation effect on RIM, we fit the exit rate as function of the RIM inhibition by the logit link function. A maximum likelihood best fit was found using the glm function in the R statistical language (R Core Team, 2014). The resulting fit is the inverse-logit (logistic) function:

$$P[y(x)] = \frac{1}{1+\exp[-y(x)]} = \frac{1}{1+\exp(-\beta_0-\beta_1 x)}\,, \tag{M4}$$

where x is the RIM inhibition and $y(x)$ is the exit rate. The parameters for the four fits, which we dub RIM inhibition coefficients, are given in the table below.

RIM inhibition coefficient	Value	Description
β_0	-3.022	Intercept, diacetyl and fructose, wild type
β_1	117.006	Coefficient, diacetyl and fructose, wild type
β_0	-0.988	Intercept, diacetyl and fructose, *tyra*-2 null
β_1	87.403	Coefficient, diacetyl and fructose, *tyra*-2 null
β_0	-6.393	Intercept, fructose, wild type
β_1	135.158	Coefficient, fructose, wild type
β_0	-3.830	Intercept, fructose, *tyra*-2 null
β_1	99.109	Coefficient, fructose, *tyra*-2 null

Experimental food deprivation data points were matched visually to RIM inhibition values by matching the percentage of wild type animals exiting the ring in the fructose only assay. If multiple RIM inhibition strengths provided an equal fit, virtual *tyra*-2 null mutant data points were used in addition to pick the best matching RIM inhibition value.

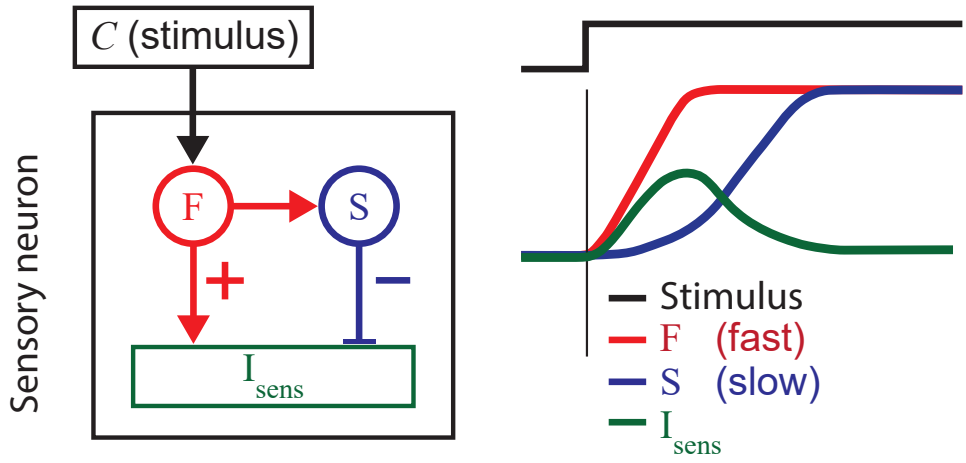

Figure M2: ***Left****: Model sensory neurons exhibit a transient response to changes in concentrations. The response is mediated by a fast component (F) that drives a slow delayed-rectifier component (S).* ***Right****: Schematic traces of the response to a concentration step change, showing the fast (F) and slow (S) components and the overall transient response (I_{sens}).*

For the assay with diacetyl and fructose, the estimates from the fructose only assay were used.

Sensory Neurons

Calcium imaging data has shown that the responses of many sensory neurons in *C. elegans* roughly approximate a low-pass filtered time derivative over their respective inputs (Hilliard et al.; Suzuki et al., 2008; Thiele et al., 2009; Kato et al., 2014; Larsch et al., 2013). In many cases, changes in stimuli selectively produce a response with a characteristic rise time, followed by a slower decay to a baseline (i.e., rest). In particular, AWA and ASH respond with a transient depolarization to stimulus upsteps, and with a transient hyperpolarization to stimulus downsteps (Thiele et al., 2009; Larsch et al., 2013). The biphasic nature of the derivative-like responses seen in AWA and ASH suggests sensory neurons use two components with opposite effect and a separation of timescales (Kato et al., 2014). Accordingly, in our model the sensory neuron response I_{sens} is given by the difference between a fast component F and a slow (delayed-rectifying) component S (Figure M2)

$$I_{\text{sens}} = F - S\,. \tag{M5}$$

The fast component F integrates over the sensory stimulus $C = C(x, y, t)$ (here the concentration of the respective signal) with a characteristic rate α_i and decays at rate β_i. The slow component S follows F with a delay, producing the characteristic biphasic response

Sensory neuron parameters	Value	Description
α_{AWA}	$4\,s^{-1}$	AWA depolarization rate
β_{AWA}	$15\,s^{-1}$	AWA depolarization leak rate
γ_{AWA}	$2\,s^{-1}$	AWA rectification (repolarization) rate
$\bar{\alpha}_{\text{ASH}}$	$4\,s^{-1}$	ASH depolarization rate
β_{ASH}	$15\,s^{-1}$	ASH depolarization leak rate
γ_{ASH}	$2\,s^{-1}$	ASH rectification (repolarization) rate

(Figure M2):

$$\frac{dF}{dt} = \alpha_i\, C - \beta_i F\,, \tag{M6}$$

$$\frac{dS}{dt} = \gamma_i (F - S)\,. \tag{M7}$$

The physiological mechanism by which TYRA-2 modulates ASH excitability is unknown. The application of tyramine did not appear to affect the ASH membrane potential. Instead, when a hyperosmotic stimulus was applied in the presence of tyramine, the ASH response appeared enhanced compared to the response in the absence of tyramine (main text Fig. 4). Consistent with these observations, here the effect of TYRA-2 on ASH excitability is modeled as a contribution to the neuronal activation rate $\bar{\alpha}_{\text{ASH}}$

$$\alpha_{\text{ASH}}(t) = \bar{\alpha}_{\text{ASH}} + T(t). \tag{M8}$$

Initially, the activity of the neurons, all neuron components and the tyramine level are set to 0.

Motor system

Model animals move at a constant speed while the direction of motion is modulated by two separate motor programs: a stochastic pirouette command unit and a central pattern generating undulation circuit consisting of two motor neurons, denoted VMN and DMN (Figure M1). Reciprocal inhibition between VMN and DMN supports a half-center oscillator that generates and maintains stable oscillations (representing the animal's undulatory locomotion). This reciprocal connectivity pattern is reminiscent of connectivity found in several classes of head motor neurons in *C. elegans*.

The oscillator subcircuit includes delayed excitatory connections (Figure M1). To simplify our model, we used 'hidden' interneurons to create a delayed connection from VMN to DMN and vice versa. Thus, the delayed excitatory connection from VMN to DMN is implemented as two connections, one from VMN to the hidden interneuron, and another from the hidden interneuron to DMN, using the neuronal time constant of the hidden interneuron (τ_m) as a synaptic delay.

In the absence of a sensory input, this subcircuit will produce stable oscillations, facilitated by fast reciprocal inhibition and delayed reciprocal excitation (Figure M1). Any activity in one of the oscillating neurons will cause fast inhibition, followed by slower excitation of the other which in turn leads to recurrent inhibition. Thus the frequency and amplitude of the oscillations are determined by the timescales of the neurons (τ_m), the

connection strengths of the reciprocal inhibition, and delay in the reciprocal excitatory connections. When both neurons are equally active, the circuit does not oscillate. However, any small difference in activity is amplified by the mutual inhibition. Thus neuronal fluctuations would ensure stable oscillations even in a symmetric circuit. For simplicity, in the model, simulations are initiated with brief, equal and opposite input pulses into the two motor neurons VMN and DMN. Input from RIM into VMN and DMN biases the undulations to mediate steering.

Similar to other computational models of *C. elegans* (Bryden and Cohen, 2004, 2008; Izquierdo and Lockery, 2010), the direction of locomotion (θ) evolves as a function of the difference of the dorsal and ventral activation:

$$\frac{d\theta}{dt} = \omega \left(V_{\mathrm{VMN}} - V_{\mathrm{DMN}} \right), \tag{M9}$$

where ω sets the undulation amplitude. Point worms move with constant velocity $v = 0.11$ mm/s along a direction vector θ according to

$$\frac{d(x,y)}{dt} = (v\ \sin\theta, v\ \cos\theta)\,. \tag{M10}$$

Pirouettes are executed by resetting the orientation of movement of the point worm θ, to a random value between 0 and 2π drawn from a uniform distribution. The probability rate of a pirouette is given by the activation of the pirouette command unit (Ω) and given by a piece-wise linear monotonic function:

$$P_\Omega(V_\Omega) = \begin{cases} \overline{V}_\Omega + \epsilon & \overline{V}_\Omega + \epsilon \leq \overline{V}_\Omega + w_\Omega\ V_\Omega \\ \overline{V}_\Omega + w_\Omega\, V_\Omega & \overline{V}_\Omega - \epsilon \leq \overline{V}_\Omega + w_\Omega\ V_\Omega < \overline{V}_\Omega + \epsilon \\ \overline{V}_\Omega - \epsilon & \overline{V}_\Omega + w_\Omega\ V_\Omega < \overline{V}_\Omega - \epsilon \end{cases} \tag{M11}$$

where V_Ω denotes the activity of the abstract pirouette neuron, $\overline{V}_\Omega$ is the mean pirouette rate (over the domain), and the proportionality constant is set to $w_\Omega = 2.1$.

Motor output	**Value**	**Description**
v	$0.11\,\mathrm{mm}\,s^{-1}$	Forward speed
V_{start}	0.001	Oscillator start signal
τ_{start}	0.01 s	Duration of oscillator start signal
w_Ω	2.1	$P_\Omega(V_\Omega)$ proportionality constant
$\overline{V}_\Omega$	$0.035\,s^{-1}$	Mean pirouette rate
ϵ	$0.035\,s^{-1}$	Pirouette rate variation amplitude

All assays are simulated on a virtual two dimensional 5 cm plate, which animals cannot leave. All coordinates are given relative to an origin at the center of the arena.

1.2 Decision making assay

A virtual decision making assay was implemented to reproduce our experimental assay. The fructose ring, $\mathrm{FR}(\vec{r}, t)$ was modeled by continuous diffusion from an initial condition of a 1 cm diameter, placed in the center of the arena. Due to the radial symmetry of the

Assay parameter	Value	Description
τ_{end}	900 s	Duration of the assay
δt	0.0001 s	Integration time step of the simulation
$\vec{r}(0) = (x(0), y(0))$	(0, 0) cm	Initial worm positions
$\theta(0)$	U(0, 2π)	initial direction drawn from uniform distribution
V_i	0	Initial activity for all neurons
F_i	0	Initial value: fast component, all sensory neurons
S_i	0	Initial value: slow component, all sensory neurons
$T(0)$	0	Initial value of Tyramine
t_{FR}	300 s	Fructose diffusion time prior to assay start
$\vec{r}_{\text{FR}} = (x_{\text{FR}}, y_{\text{FR}})$	(0, 0) cm	Center of fructose ring
R	0.5 cm	Fructose ring radius
D_{FR}	3×10^{-5} cm^2/s	Fructose ring diffusion coefficient
C_{FR}	20, 30, 40	Fructose coefficients for 2, 3 and 4 M respectively
t_{DA}	60 s	Diacetyl diffusion time prior to assay start
$\vec{r}_{\text{DA}}^{1,2} = (x_{\text{DA}}^{1,2}, y_{\text{DA}}^{1,2})$	$(\pm 1.5, 0)$ cm	Center of diacetyl spots
D_{DA}	2.52×10^{-4} cm^2/s	Diacetyl diffusion coefficient
C_{DA}	100	Diacetyl amplitude

problem, assuming an initial narrow ring at R and neglecting the boundary conditions at the edge of the plate, the exact solution to the fructose diffusion in two dimensions is given by

$$\mathrm{C}(\vec{r}, t) = M_0 \int_0^\infty d\lambda \; \lambda \, e^{-\lambda^2 D_{\text{FR}} \, t} J_0(\lambda R) \, J_0(\lambda r) \,, \tag{M12}$$

where $r = |\vec{r}|$, J_0 is the zeroth regular Bessel function and M_0 is a normalization constant. Sufficiently close to the ring, the solution is well approximated by a one dimensional diffusion along the polar coordinate r:

$$\mathrm{FR}(r, t) = C_{\text{FR}} \left(\frac{t_{\text{FR}}}{t_{\text{FR}} + t} \right)^{\frac{1}{2}} \left(\exp\left[-\frac{(r-R)^2}{4 D_{\text{FR}} (t_{\text{FR}} + t)} \right] + \exp\left[-\frac{(r+R)^2}{4 D_{\text{FR}} (t_{\text{FR}} + t)} \right] \right) . \tag{M13}$$

Here t_{FR} denotes the time of fructose diffusion prior to the start of the experiment at $t = 0$, when virtual worms are added to the simulation. The coefficient C_{FR} incorporates the concentration, diffusion coefficient factor and sensory neuron receptor strengths, and is referred to for simplicity as a concentration. The two exponentials correspond to contributions from the two edges of the ring: The closer edge at a distance $r - R$ from the worm and the farther edge at a distance $r + R$. The concentration and diffusion coefficient were set to match experimental results with different durations of fructose diffusion t_{FR}.

Visual inspection of experimental worm traces showed animals moving towards diacetyl peaks even after 15 minutes. This is consistent with continuing evaporation of diacetyl, leading to an sustained concentration gradient throughout the assay. To capture this, we approximated the diacetyl concentration profile $\mathrm{DA}(x, y, t)$, by a two phased process: an initial rapid diffusion (to establish the concentration profile from two initial spots), followed by a static field:

$$\mathrm{DA}(x, y, t) = C_{\text{DA}} \sum_{i=1}^{2} \exp\left(-\frac{(x - x_{\text{DA}}^i)^2 + (y - y_{\text{DA}}^i)^2}{4 D_{\text{DA}} \, t_{\text{DA}}} \right) , \tag{M14}$$

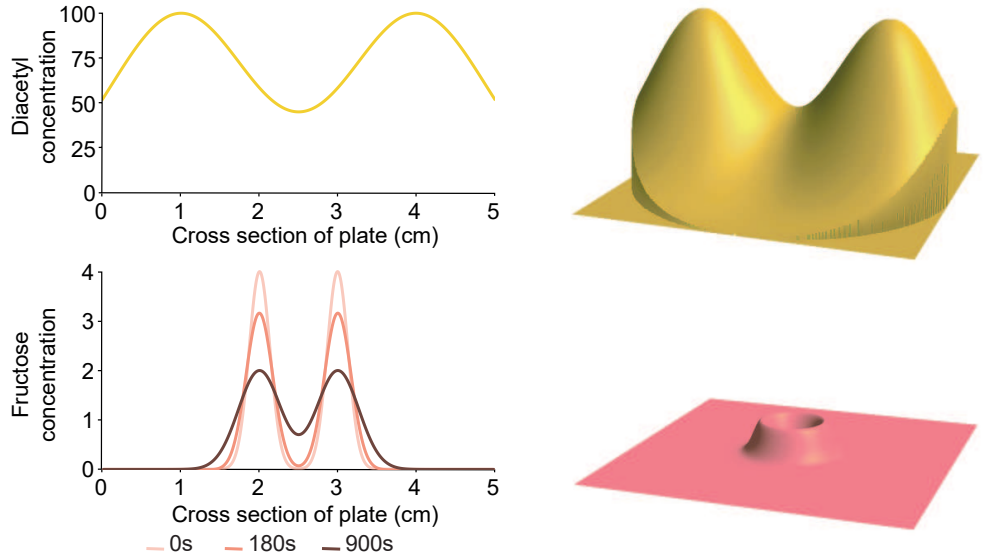

Figure M3: *Concentration profiles (cross sections and corresponding top-down views) used in the* in silico *decision making assay.* ***Top:*** *Steady state diacetyl profile resulting from two diacetyl sources at* ± 1.5 *cm from the center.* ***Bottom:*** *Snapshots of fructose concentration profile due to diffusion from a 1 cm diameter ring.*

where $(x^i_{\mathrm{DA}}, y^i_{\mathrm{DA}})$ are the coordinates for the i^{th} diacetyl spot and t_{DA} denotes the duration of diacetyl diffusion.

At $t = 0$ a single worm is placed at the center of the arena. Numerical integration of its nervous system and motor control is implemented with Euler integration, with a fixed integration time step (0.1 ms). As in the experimental assay, the balance of attraction and repulsion was quantified by the percentage of independently simulated worms that have exited the ring by 900 seconds.

References

J. Bryden and N. Cohen. Neural control of *Caenorhabditis elegans* forward locomotion: the role of sensory feedback. *Biological Cybernetics*, 98(4):339–351, 2008. doi: 10.1007/s00422-008-0212-6.

J. A. Bryden and N. Cohen. A simulation model of the locomotion controllers for the nematode *Caenorhabditis elegans*. In S. Schaal, A. Ijspeert, A. Billard, S. Vijayakumar, J. Hallam, and J.-A. Meyer, editors, *From Animals to Animats 8: Proceedings of the Eighth International Conference on the Simulation of Adaptive Behavior*, pages 183–192, July 2004.

M. A. Hilliard, A. J. Apicella, R. Kerr, H. Suzuki, P. Bazzicalupo, and W. R. Schafer. *In vivo* imaging of *C. elegans* ash neurons: cellular response and adaptation to chemical repellents. *EMBO Journal*, 24.

R. K. Hukema, S. Rademakers, M. P. J. Dekkers, J. Burghoorn, and G. Jansen. Antagonistic sensory cues generate gustatory plasticity in *Caenorhabditis elegans*. *EMBO Journal*, 25:312–322, 2006.

R. K. Hukema, S. Rademakers, and G. Jansen. Gustatory plasticity in *C. elegans* involves integration of negative cues and nacl taste mediated by serotonin, dopamine, and glutamate. *Learning and Memory*, 15:829–836, 2008.

Y. Iino and K. Yoshida. Parallel use of two behavioral mechanisms for chemotaxis in *Caenorhabditis elegans*. *The Journal of Neuroscience*, 29:5370–5380, 2009.

E. J. Izquierdo and S. R. Lockery. Evolution and analysis of minimal neural circuits for klinotaxis in *Caenorhabditis elegans*. *The Journal of Neuroscience*, 30:12908–12917, 2010.

G. Jansen, D. Weinkove, and R. H. A. Plasterk. The g-protein gamma subunit gpc-1 of the nematode *C. elegans* is involved in taste adaptation. *EMBO Journal*, 21:986–994, 2002. doi: 10.1093/emboj/21.5.986.

S. Kato, Y. Xu, C. E. Cho, L. F. Abbott, and C. I. Bargmann. Temporal responses of *C. elegans* chemosensory neurons are preserved in behavioral dynamics. *Neuron*, 81(3): 616–628, 2014.

J. Larsch, D. Ventimiglia, C. I. Bargmann, and D. R. Albrecht. High-throughput imaging of neuronal activity in *Caenorhabditis elegans*. *Proceedings of the National Academy of Sciences of the United States of America*, 110(45):E4266–E4273, 2013. doi: 10.1073/pnas.1318325110.

R Core Team. *R: A Language and Environment for Statistical Computing*. R Foundation for Statistical Computing, Vienna, Austria, 2014. URL `http://www.R-project.org/`.

H. Suzuki, T. R. Thiele, S. Faumont, M. Ezcurra, S. R. Lockery, and W. R. Schafer. Functional asymmetry in *Caenorhabditis elegans* taste neurons and its computational role in chemotaxis. *Nature*, 454(7200):114–117, 2008. doi: 10.1038/nature06927.

T. R. Thiele, S. Faumont, and S. R. Lockery. The neural network for chemotaxis to tastants in *Caenorhabditis elegans* is specialized for temporal differentiation. *The Journal of Neuroscience*, 29(38):11904–11911, 2009.

J. G. White, E. Southgate, J. N. Thomson, and S. Brenner. The structure of the nervous system of the nematode *C. elegans*. *Philosophical Transactions of the Royal Society London B Biological Sciences*, 314(1165):1–340, 1986.

Click here to access/download

Supplemental Movies & Spreadsheets

vid_0000_4--sent_sanders--8-28-16.mp4